PRUSSIC III. ALMA and NOEMA survey of dense gas in high-redshift star-forming galaxies

A&A, 706, A69 (2026)
https://doi.org/10.1051/0004-6361/202556845

Astronomy & Astrophysics

PRUSSIC

III. ALMA and NOEMA survey of dense gas in high-redshift star-forming galaxies

M. Rybak[1,2,3,⋆], G. Sallaberry[1], J. A. Hodge[1], D. Riechers[4], N. N. Geesink[1,5], T. R. Greve[6,7,8], S. Viti[1,9], F. Walter[10], P. P. van der Werf[1], and C. Yang[11]

[1] Leiden Observatory, Leiden University, P.O. Box 9513, 2300 RA Leiden, The Netherlands
[2] Faculty of Electrical Engineering, Mathematics and Computer Science, Delft University of Technology, Mekelweg 4, 2628 CD Delft, The Netherlands
[3] SRON – Netherlands Institute for Space Research, Niels Bohrweg 4, 2333 CA Leiden, The Netherlands
[4] Institut für Astrophysik, Universität zu Köln, Zülpicher Straße 77, D-50937 Köln, Germany
[5] European Southern Observatory (ESO), Karl-Schwarzschild-Straße 2, Garching 85748, Germany
[6] Cosmic Dawn Center (DAWN), København, Denmark
[7] DTU–Space, Technical University of Denmark, Elektrovej 327, 2800 Kgs. Lyngby, Denmark
[8] Department of Physics and Astronomy, University College London, Gower Street, London WC1E 6BT, United Kingdom
[9] Transdisciplinary Research Area (TRA) ´Matter´/Argelander-Institut für Astronomie, University of Bonn, Bonn, Germany
[10] Max–Planck Institut für Astronomie, Königstuhl 17, 69117 Heidelberg, Germany
[11] Department of Space, Earth and Environment, Chalmers University of Technology, SE-412 96 Gothenburg, Sweden

Received 13 August 2025 / Accepted 4 November 2025

ABSTRACT

Characterising the relationship between dense gas and star formation is critical for understanding the assembly of galaxies throughout cosmic history. However, due to the faintness of standard dense-gas tracers – HCN, HCO^+, and HNC – dense gas in high-redshift galaxies remains largely unexplored. We present ALMA and NOEMA observations targeting HCN/HCO^+/HNC (3–2) and (4–3) emission lines in 11 (mostly) gravitationally lensed dusty star-forming galaxies (DSFGs) at redshift $z = 1.6–3.2$. We detect at least one line in 10 out of 11 galaxies. Altogether, we detect 34 dense-gas transitions, more than quadrupling the number of extant high-redshift detections. Additionally, in two targets, we detect lower-abundance CO isotopologues ^{13}CO and C^{18}O, as well as CN emission. We derive excitation coefficients for HCN, HCO^+, and HNC in DSFGs, finding them to be systematically higher than those in nearby luminous infrared galaxies. Assuming the canonical dense-mass conversion factor ($\alpha_{HCN} = 10$), we find that DSFGs have shorter dense-gas depletion times (median 23 Myr) than nearby galaxies (≈60 Myr), with a star-forming efficiency per free-fall time of 1–2%, a factor of a few higher than in local galaxies. We find a wide range of dense-gas fractions, with HCN/CO ratios ranging between 0.01 and 0.15. Finally, we put the first constraints on the redshift evolution of the cosmic dense-gas density, which increases by a factor of 7 ± 4 between $z = 0$ and $z = 2.5$, consistent with the evolution of the cosmic molecular-gas density.

Key words. ISM: molecules – galaxies: high-redshift – galaxies: ISM – galaxies: star formation – submillimeter: galaxies

1. Introduction

Understanding the process of star formation – how the cold, molecular gas is converted into newborn stars – is one of the key questions in astrophysics. Present-day galaxies, on average, convert gas into stars inefficiently, depleting their gas over billions of years (e.g. Tacconi et al. 2018, 2020). However, in the early Universe, the star-forming activity was much higher, peaking between redshifts $z = 1–4$ (e.g. Madau & Dickinson 2014; Zavala et al. 2021; Harikane et al. 2023), during the so-called "Cosmic Noon". This intense star formation is dominated by massive, dusty star-forming galaxies (DSFGs[1]), which were producing stars at rates up to a hundred times higher than present-day galaxies (e.g. Magnelli et al. 2011; Dudzevičiūtė et al. 2020; Zavala et al. 2021).

This trend is qualitatively matched by the evolution of molecular gas density, based on surveys of low-J CO, [C II], [C I], and cold dust emission, primarily with the NOrthern Extended Millimeter Array (NOEMA) and Atacama Large Millimeter/Sub-millimeter Array (ALMA) (e.g. Riechers et al. 2019; Walter et al. 2020; Hodge & da Cunha 2020; Tacconi et al. 2020; Bollo et al. 2025 and references therein). These studies have shown that the elevated star-forming activity at the Cosmic Noon is primarily due to the increase in the molecular gas content of galaxies, with only a mild increase in star-forming efficiency (by a factor of ≈3).

However, these large-volume average trends provide a potentially biased view of the actual star-forming processes in high-redshift galaxies. First, while conveniently bright, CO, [C II], [C I], and dust continuum trace gas across a wide range of densities (down to $\approx 100\,cm^{-3}$ for [C II]), rather than the dense gas from which stars actually form ($n \geq 10^4\,cm^{-3}$). Moreover, spatially resolved observations of [C II] (e.g. Gullberg et al. 2018; Rybak et al. 2019, 2020; Fujimoto et al. 2020; Ginolfi et al. 2020; Ikeda et al. 2025) and CO(1–0) emission (e.g. Ivison et al. 2011; Riechers et al. 2011; Stanley et al. 2023; Rybak et al. 2025) indicate that the majority of cold gas (up to ≈80%,

⋆ Corresponding author: mrybak@strw.leidenuniv.nl

[1] In this work, we consider DSFGs to have continuum flux at 850-μm (observed-frame) $S_{850\,\mu m} \geq 1$ mJy.

Rybak et al. 2025) is in extended, diffuse halos and does not directly contribute to the observed star-forming activity. Finally, theoretical studies suggest that the bulk of cold, molecular gas might reside in low-mass, sub-mm faint galaxies, rather than high-mass, sub-mm bright galaxies that dominate the star-forming activity at the Cosmic Noon (e.g. Lagos et al. 2020).

To properly understand the star-forming processes in high-redshift galaxies, we need to characterise the relationship between their dense gas[2] and star formation. Tracing dense gas requires observations of spectral lines of molecules that have high critical densities – particularly HCN, HCO^+, and HNC, whose ground-state rotational transitions have critical densities of $n_{crit} = 13 \times 10^5$, 1.9×10^5, and 3×10^5 cm^{-3} at a temperature of $T = 20$ K, respectively.

Indeed, surveys of local galaxies have established HCN(1–0) as the 'gold-standard' tracer of dense gas (see, e.g. recent reviews by Saintonge & Catinella 2022; Schinnerer & Leroy 2024). The HCN(1–0) luminosity and star-formation rate correlate linearly over ∼8 orders of magnitude, from individual molecular clouds (e.g. Wu et al. 2005; Kauffmann et al. 2017; Dame & Lada 2023; Forbrich et al. 2023) to entire galaxies (e.g. Nguyen et al. 1992; Gao & Solomon 2004b; Graciá-Carpio et al. 2008; García-Burillo et al. 2012; Costagliola et al. 2011) and sub-galactic scales (e.g. Bigiel et al. 2015; Gallagher et al. 2018; Jiménez-Donaire et al. 2019; Neumann et al. 2023; Stuber et al. 2025). Compared to HCN, HCO^+ and HNC are more sensitive to gas thermodynamics. For example, HCO^+ is sensitive to the free-electron abundance (e.g. Papadopoulos 2007), while HNC abundance depends on gas temperature due to its temperature-sensitive formation and destruction pathways (e.g. Hacar et al. 2020).

Extending local studies of dense-gas tracers to high redshift remains challenging, as the HCN/HCO^+/HNC emission can be more than 10× fainter than CO. Additionally, at high redshift, the ground-state HCN/HCO^+/HNC lines move into the high-frequency bands of Karl G. Jansky Very Large Array (JVLA), which can be used only under good weather conditions. As a result, to date, "there have been no systematic studies of HCN (or other high-dipole-moment molecules) at high-z, but in principle these are now feasible with the capabilities of ALMA and NOEMA" (Tacconi et al. 2020, p. 168). In fact, despite almost two decades of effort, there are only three $z \geq 1$ DSFGs detected in the HCN(1–0) emission[3] (Gao et al. 2007; Oteo et al. 2017; Rybak et al. 2022). Indeed, as shown by the recent JVLA survey of Rybak et al. (2022), DSFGs might have low dense-gas fractions, making HCN(1–0) emission even harder to detect.

An alternative to observing the ground-state transitions are the mid-J rotational HCN/HCO^+/HNC lines. These are both intrinsically brighter than the ground-state transitions and at $z \geq 1$ fall conveniently into the easily accessible 2-mm and 3-mm atmospheric windows. The mid-J HCN lines have been proposed to be better tracers of dense gas than HCN(1–0) (Viti 2017), but their interpretation is more complex, as they might be sensitive to, e.g. shock heating, and mid-IR pumping (Aalto et al. 2007; Kazandjian et al. 2015).

In local galaxies, the HCN/HCO^+/HNC (3–2) and (4–3) lines have been systematically targeted from the scales of entire galaxies (Baan et al. 2008; Bussmann et al. 2008; Graciá-Carpio et al. 2008; Krips et al. 2008; Zhang et al. 2014; Imanishi et al. 2018a; Israel 2023) to sub-kiloparsec scales (Wilson et al. 2008; Tan et al. 2018; Nishimura et al. 2024; Butterworth et al. 2025) and parsec scales (e.g. Imanishi et al. 2018b; Impellizzeri et al. 2019). In contrast, only a handful of $z \geq 1$ DSFGs have been detected in the $J_{upp} = 3$, 4, and 5 emission lines (Danielson et al. 2013; Oteo et al. 2017; Béthermin et al. 2018; Cañameras et al. 2021; Yang et al. 2023), alongside several quasars (Wagg et al. 2005; Riechers et al. 2010). Even spectral stacking studies have yielded only a handful of HCN/HCO^+(4–3) detections (Spilker et al. 2014; Reuter et al. 2023; Hagimoto et al. 2023). However, stacking studies only cover $J_{upp} \geq 3$ lines and miss anchoring to low-J emission lines.

Converting these mid-J HCN detections to dense-gas masses requires knowing the HCN spectral line energy distribution. However, the excitation of dense-gas tracers is almost completely unconstrained. Even in local galaxies, HCN/HCO^+/HNC ladders have been largely unexplored, with only a handful of studies dedicated to the topic (e.g. Krips et al. 2008; Papadopoulos et al. 2014; Israel 2023). At high redshift, just one DSFG has been detected in both the ground-state and a mid-J HCN transition: SDP.9 ($z = 1.575$), which was detected in HCN(1–0) and HCN(3–2) by Oteo et al. (2017). The stacking studies are not helpful in this regard, as they do not cover the ground-state transition. Moreover, different transitions – e.g. HCN(3–2) and (4–3) lines – arise from different galaxies, which can hide the true scatter of the excitation ratios (see a recent work on CO excitation by Frias Castillo et al. 2023).

PRUSSIC[4] is a comprehensive census of dense-gas tracers in high-redshift star-forming galaxies, aiming to drastically expand the number of high-redshift galaxies detected in dense-gas tracers. In the first PRUSSIC paper, Rybak et al. (2022, Paper I) have presented the JVLA observations of the $J_{upp} = 1$ HCN, HCO^+, and HNC emission in six $z \sim 3$ lensed DSFGs, finding low dense-gas fractions and elevated dense-gas star-forming efficiencies. The second paper (Rybak et al. 2023, Paper II) presented ALMA imaging of the HCN, HCO^+, and HNC $J_{upp} = 4$ lines in a $z \approx 3$ lensed DSFG SDP.81, finding an unusually high HCO^+/HCN ratio, indicating a subsolar metallicity and low mechanical heating.

In this third paper of the PRUSSIC series, we present observations of the mid-J HCN/HCO^+/HNC emission in 11 redshift[5] $z = 1.6$–3.2 lensed star-forming galaxies, obtained with ALMA and NOEMA. This paper is structured as follows. In Section 2, we present the targeted galaxies, details of NOEMA and ALMA observations, and data reduction. Section 3 presents the resulting continuum (Sect. 3.1) and line measurements (Sect. 3.2). In Section 4, we place our observations in the context of low- and high-redshift surveys of dense gas (Sect. 4.1), discuss the HCN/HCO^+/HNC line width (Sect. 4.2) and ratios (Sect. 4.3), present the dense-gas excitation ladders (Sect. 4.4), derive the star-forming efficiencies (Sect. 4.5), place constraints on the redshift evolution of the dense-gas content of galaxies (Sect. 4.6), and discuss the underlying systematics (Sect. 4.7).

[2] While the definition of 'dense' gas is arbitrary, following Gao & Solomon (2004a), we consider gas with $n \geq 3 \times 10^4$ cm^{-3} as dense.

[3] In addition to these star-formation dominated galaxies, several high-z QSOs have been detected in the HCN(1–0) (Solomon et al. 2003; Vanden Bout et al. 2004; Carilli et al. 2005) or HCO^+(1–0) (e.g. Riechers et al. 2006).

[4] Prussic acid is an alternative name for HCN, which was first isolated from the Prussian blue pigment.

[5] Throughout this paper, we assume a flat ΛCDM cosmology, with $\Omega_m = 0.315$ and $H_0 = 67.4$ km s^{-1} Mpc^{-1} (Planck Collaboration XIII 2016), and the Salpeter initial stellar mass function (IMF, Salpeter 1955).

Table 1. Target galaxies and their properties, ordered by increasing redshift.

Source	RA & Dec [J2000]	z_s	z_L	$L_{\rm FIR}^{\rm sky}$ [$10^{12}\,L_\odot$]	$L'^{\rm sky}_{\rm CO(1-0)}$ [10^{10} K km s^{-1} pc^{-2}]	FWHM CO(1−0) [km/s]	$\mu_{\rm FIR}$
SDP.9	09:07:40.0 –00:41:59.8	1.575	0.613	$66 \pm 1^{\rm O17}$	$13 \pm 3^{\rm O17}$	370 ± 10^{a}	$8.8 \pm 2.2^{\rm B13}$
SDP.11	09:10:43.1 –00:03:22.8	1.786	0.793	$64 \pm 1^{\rm O17}$	$13 \pm 1^{\rm O17}$	$500 \pm 100^{\rm O17}$	$10.9 \pm 1.3^{\rm B13}$
G09v1.40	08:53:58.9 +01:55:37.7	2.092	?^{b}	$66 \pm 25^{\rm Y17}$	$30 \pm 8^{\rm Y17}$	$310 \pm 90^{\rm Y17,c}$	$15.3 \pm 3.5^{\rm B13}$
SDP.17	09:03:03.0 –01:41:27.1	2.305	0.23	$71 \pm 26^{\rm Y17}$	$26 \pm 3^{\rm H12}$	$1000 \pm 130^{\rm H12}$	$4.9 \pm 0.7^{\rm B13}$
J1202	12:02:07.6 +53:34:39	2.442	0.21	$81 \pm 4^{\rm H21}$	$142 \pm 50^{\rm H21}$	600 ± 20^{d}	$25.0^{\rm H21,d}$
G15v2.235	14:13:52.1 –00:00:24.4	2.478	0.547	$28 \pm 7^{\rm Y17}$	$43 \pm 5^{\rm H12}$	$500 \pm 40^{\rm H12}$	$1.8 \pm 0.3^{\rm B13}$
J0209	02:09:41.3 +00:15:59	2.553	0.20	$133 \pm 4^{\rm H21}$	$84 \pm 11^{\rm R}$	410 ± 20^{e}	14.7 ± 0.3
G09v1.326	09:18:40.9 +02:30:45.9	2.581	–	$40 \pm 5^{\rm H12}$	$33 \pm 8^{\rm H12}$	$680 \pm 140^{\rm H12}$	1
SDP.130	09:13:05.4 –00:53:41	2.625	0.22	$32 \pm 3^{\rm B13}$	$25 \pm 4^{\rm F11}$	$360 \pm 40^{\rm F11}$	$8.6 \pm 0.4^{\rm F18}$
NAv1.195	13:26:30.2 +33:44:07.6	2.951	0.785	$75 \pm 20^{\rm Y17}$	$57 \pm 20^{\rm H21}$	$266 \pm 19^{\rm H21}$	$4.1 \pm 0.3^{\rm F18}$
SDP.81	09:03:11.6 +00:39:07	3.042	0.299	$43 \pm 1^{\rm R20}$	$54 \pm 9^{\rm V11}$	$435 \pm 54^{\rm V11}$	$18.2 \pm 1.2^{\rm R20}$
G12v2.43	11:35:26.3 –01:46:06.6	3.128	?^{b}	$90 \pm 2^{\rm Y17}$	$15 \pm 3^{\rm H12}$	$350 \pm 80^{\rm H12}$	$9.2 \pm 3.2^{\rm G23,f}$

Notes. Individual columns list the source position, source and lens redshift (z_S, z_L), sky-plane (lensed) FIR and CO(1–0) luminosities, CO(1–0) FWHM and FIR continuum magnification. $L_{\rm FIR}$ is inferred from modified black-body fits integrated over 8−1000 µm. For completeness, we also include SDP.81 from Paper II (Rybak et al. 2023). [a] – derived from the CO(3–2) lines from our NOEMA observations. [b] – For G09v1.40 and G12v2.43, z_L are unknown. [c] – Derived from CO(2–1), assuming CO is thermalised. [d] – No lens model available. [e] – derived from ALMA observations, Project ID #2023.1.00432.S (PI: M. Rybak). [f] – Mean magnification for ALMA Bands 6, 7, and 8 continuum (Giulietti et al. 2023). References: B13 – Bussmann et al. (2013), F11 – Frayer et al. (2011), F17 – Falgarone et al. (2017), G23 – Giulietti et al. (2023), H12 – Harris et al. (2012), H21 – Harrington et al. (2021), I12 – Iono et al. (2012), O17 – Oteo et al. (2017), R – Riechers et al. (in prep.); R20 – Rybak et al. (2020), V11 – Valtchanov et al. (2011), Y17 – Yang et al. (2017).

2. Targets, observations, and imaging

2.1. Target sample

Our sample comprises eleven DSFGs at z = 1.6−3.1 (median z = 2.52), i.e. 2.1−4.1 Gyr after the Big Bang. The targets are drawn from the *Herschel* H-ATLAS survey (Negrello et al. 2010, 2017), and the *Planck* sample of strongly lensed DSFGs (Cañameras et al. 2015; Harrington et al. 2021).

The intrinsic (magnification-corrected) far-infrared luminosity spans almost 1 dex ($L_{\rm FIR}$ = 2.5 × 10^{12}–2.2 × $10^{13}\,L_\odot$; median: 1.0 × $10^{13}\,L_\odot$), which corresponds to a star-formation rate SFR = 400–4000 $M_\odot\,{\rm yr}^{-1}$ (median SFR = 1800 $M_\odot\,{\rm yr}^{-1}$). The targeted DSFGs thus include both extremely star-forming systems, as well as more "normal" galaxies at these redshifts. We list the properties of individual galaxies in Table 1.

Five galaxies from our sample were observed with NOEMA, while six additional sources were observed by ALMA. SDP.130 was observed by both NOEMA ($J_{\rm upp}$ = 3 lines) and ALMA ($J_{\rm upp}$ = 4 lines). Five galaxies (including SDP.130) were targeted in both $J_{\rm upp}$ = 3 and 4 transitions. Finally, for completeness, we also include ALMA observations of SDP.81, previously presented in Paper II.

2.2. NOEMA observations and calibration

The observations were carried out under the NOEMA projects S21CB and S23CB (PI: M. Rybak). In total, five sources were observed: SDP.9, SDP.11, J0209, J1202, and SDP.130. The S21CB observations were carried out between June 2021 and January 2022. The S23CB observations were carried out in October 2023. The array consisted of 9 to 12 antennas with 15 m diameter deployed in either D (the most compact) or C configuration. All observations were taken in the standard wideband mode, with two 7.744-GHz sidebands and spectral resolution of 2 MHz. As the observations spanned both summer and winter semesters, the precipitable water vapour (pwv) varied considerably between individual scheduling blocks, from ∼2 mm to ∼12 mm. Details of the NOEMA observations are given in Appendix A.

The NOEMA data were calibrated and reduced using the GILDAS package[6]. We used the new baseline-based amplitude calibration where applicable. Tracks for J0209 and SDP.130 showed some shadowing at low elevations; we manually flagged the shadowed antennas. Additionally, we tried to further improve the data fidelity by using self-calibration; however, this did not yield an appreciable increase in the signal-to-noise ratio (S/N). The data presented below are thus not self-calibrated. The resulting beam size FWHM varied from 2.6″ × 0.9″ to 7.5″ × 5.0″.

2.3. ALMA observations and calibration

We supplemented our NOEMA observations with archival ALMA data from project 2017.1.01694.S (PI: I. Oteo). This project targeted a total of eight lensed DSFGs discovered in *Herschel* surveys. Seven sources were targeted in the $J_{\rm upp}$ = 4 transitions, while G09v1.40 (which is at a lower redshift than the rest of the sample) was observed in the $J_{\rm upp}$ = 3 transitions. Data for SDP.81 have been recently presented in Rybak et al. (2023), here we present the remaining seven sources.

The observations were carried out between 2018 March 30 and 2018 May 1 using ALMA Band 3 receivers. The time on-source ranged between 0.5 and 1.7 hours. The baselines ranged between 15 and 500 m for all sources but NAv1.195, for which baselines out to 740 m were used. The spectral setup consisted of a single sideband with two spectral windows, each with 128 channels with a frequency resolution of 31.250 MHz. The other sideband was not used.

We processed the data using the standard ALMA pipeline; the data quality was generally excellent. The resulting beam size FWHM varied from 2.1″ × 1.6″ to 2.7″ × 2.1″.

[6] https://www.iram.fr/IRAMFR/GILDAS/

2.4. Imaging procedure

We imaged the data using CASA's `tclean` task. To maximise the sensitivity, we used natural weighting for all images. We used a pixel size of $0.1'' \times 0.1''$, ensuring that the synthesised beam is properly sub-sampled (see Table A.1).

For both NOEMA and ALMA data, we first identified potential line emission by examining dirty-image cubes. The resulting cubes had a default channel spacing of 20 MHz; in case these did not show any signal, we re-imaged the data using a coarser resolution of 100 MHz. We then created wide-band continuum images excluding channels with emission lines. For NOEMA, we created separate continuum images for the upper/lower sideband.

In the next step, we subtracted the continuum signal by fitting a constant function to the line-free channels using CASA's `uvcontsub` task. We then extracted spectra for each source using hand-drawn apertures corresponding to the 2σ contour in continuum maps; these are presented in Fig. 1. Finally, we created narrow-band images of each line by imaging the channels within ±0.5 FWHM of the low-J CO line (Table 1). We performed the deconvolution manually, with a stopping threshold of 1.5σ.

To derive the line fluxes, we created narrow-band images over ±0.5 FWHM of the linewidth of the lowest-J CO line available (Fig. 2). For a Gaussian profile, this range should include 76% of the total line flux; we corrected the inferred total line luminosities accordingly. We preferred this approach to fitting parametric profiles to the spectra, as the lines might not follow exactly a Gaussian profile (see Section 4.2).

3. Results

3.1. Continuum emission

We first examined the continuum images for individual sources (Figs. B.1 and B.2), which corresponds to rest-frame wavelengths 845 µm or 1.1 mm. All NOEMA targets are marginally resolved. In the ALMA imaging, G09v1.326 and NAv1.195 are resolved into two separate components; SDP.130 is marginally resolved, with a small extension to the south-west, which is arising from a source at a lower redshift (Falgarone et al. 2017). For the lensed sources, a significant fraction of the observed 2-mm or 3-mm continuum might arise from AGNs in the foreground lensing galaxies, such as seen in ALMA Band 3 observations of SDP.81 (Rybak et al. 2023).

3.2. HCN, HCO$^+$, and HNC emission

Figure 2 shows the narrow-band images at the positions of HCN, HCO$^+$, and HNC lines. We detect HCN/HCO$^+$/HNC (3−2) emission lines in all targeted galaxies except SDP.130, and HCN/HCO$^+$/HNC (4−3) emission lines in seven out of nine targets. The two sources without any line detections are G09v1.326 and G15v2.235. Additionally, J1202 is not detected in the HNC(4–3) line, while SDP.130 is not detected in the HCO$^+$(4–3) line (Rybak et al. 2023). The inferred line luminosities (or 3σ upper limits) are listed in Table 2. We provide details on the detections of CO isotopologues and CN(3–2) lines in Appendices C and D.

4. Discussion

4.1. Dense-gas tracer scaling relations

We now compare our HCN, HCO$^+$, and HNC observations to previous observations of local and high-redshift galaxies. Figure 3 presents our data in the context of $z = 0$ resolved (Tan et al. 2018; Li et al. 2020) and galaxy-averaged measurements (Greve et al. 2009; Krips et al. 2008; Greve et al. 2009; Papadopoulos et al. 2014; Zhang et al. 2014; Nishimura et al. 2024). Additionally, we compare our observations to the empirical power-law scaling relations of Nishimura et al. (2024) and Zhang et al. (2014).

However, the Nishimura et al. (2024) relations were derived over a narrow range of $L_{\rm FIR} = (1-15) \times 10^{11}\ L_\odot$ and do not provide a good fit to data at higher and lower FIR luminosities. We therefore re-fit[7] the HCN(3–2) and HCO$^+$(3–2) data using a power-law model, fitting data from Krips et al. (2008), Li et al. (2020), Nishimura et al. (2024) and our high-z measurements. We obtain:

$$\log L_{\rm FIR} = (0.91 \pm 0.05) \times \log L'_{\rm HCN(3-2)} + (3.70 \pm 0.44), \quad (1)$$

and

$$\log L_{\rm FIR} = (1.04 \pm 0.09) \times \log L'_{\rm HCO^+(3-2)} + (3.90 \pm 0.54). \quad (2)$$

The slopes for HCN(3–2) and HCO$^+$(3–2) are close to unity (within $1-2\sigma$). The almost-linear slopes contrast with predictions for sub-linear correlation from older theoretical work (Krumholz & Thompson 2007; Narayanan et al. 2008) and surveys of local galaxies (e.g. Bussmann et al. 2008; Juneau et al. 2009, who found slopes of ≈0.7 for the log($L_{\rm FIR}$)–log ($L'_{\rm HCN(3-2)}$)' Juneau et al. 2009).

For the $J_{\rm upp} = 4$ lines, we consider the Zhang et al. (2014) relations[8], which were derived using spatially unresolved observations of nearby galaxies:

$$\log L_{\rm FIR} = (1.00 \pm 0.04) \times \log L'_{\rm HCN(4-3)} + (3.67 \pm 0.28) \quad (3)$$

and:

$$\log L_{\rm FIR} = (1.12 \pm 0.05) \times \log L'_{\rm HCO^+(4-3)} + (2.83 \pm 0.34). \quad (4)$$

As is shown in Fig. 3, all our measurements are consistent with the Zhang et al. (2014) $L_{\rm FIR}$–HCN(4–3) trend within the $\pm 1\sigma$, similar to the single detection from Cañameras et al. (2021) and stacking results from Reuter et al. (2023). Similar to the HCN/HCO$^+$(3–2) lines, the linear slopes inferred from the data contrast with predictions from Narayanan et al. (2008) who predicted a slope of ≈0.6.

While the HCN(4–3) luminosities in our DSFGs scatter equally above and below the Zhang et al. (2014) trend, they are slightly overluminous in HCO$^+$(4–3), although still within the 1σ scatter. We provide a more detailed discussion of line ratios in Fig. 4. We do not show the corresponding plots for the HNC lines due to the paucity of $z \approx 0$ measurements.

4.2. Linewidths of dense-gas tracers vs CO

We now investigate whether linewidths of dense-gas tracers differ significantly from those of low-J CO lines, which trace the

[7] We fit the data in the log-log space using the LINMIX package (Kelly 2007) which explicitly includes non-detections.

[8] The original fit from Zhang et al. (2014, p. 4) contains a typo; we give the correct form (Z. Zhang, priv. comm.).

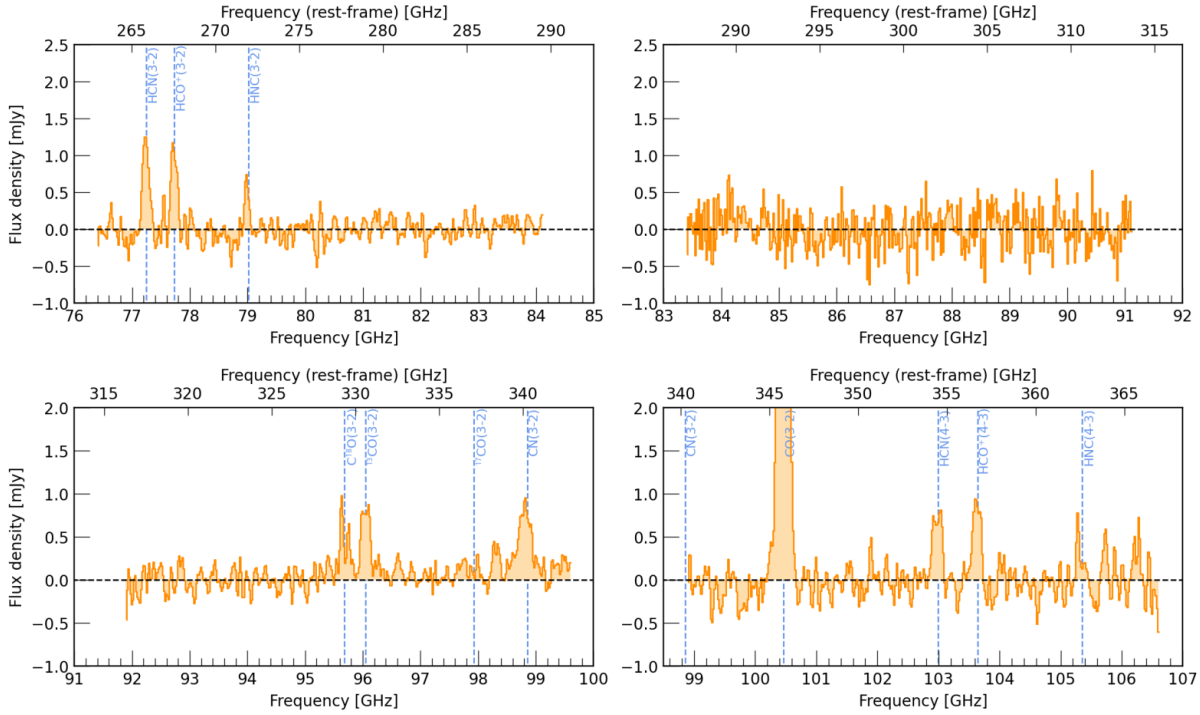

Fig. 1. NOEMA Band-1/2 spectra for J1202. We detect the HCN, HCO^+, HNC (3–2) and (4–3) lines, alongside the CO(3–2) isotopologues and CN(3–2). The HNC(3–2) and (4–3) line profiles differ significantly from those of HCN and HCO^+. See Appendix B for the spectra of remaining targets.

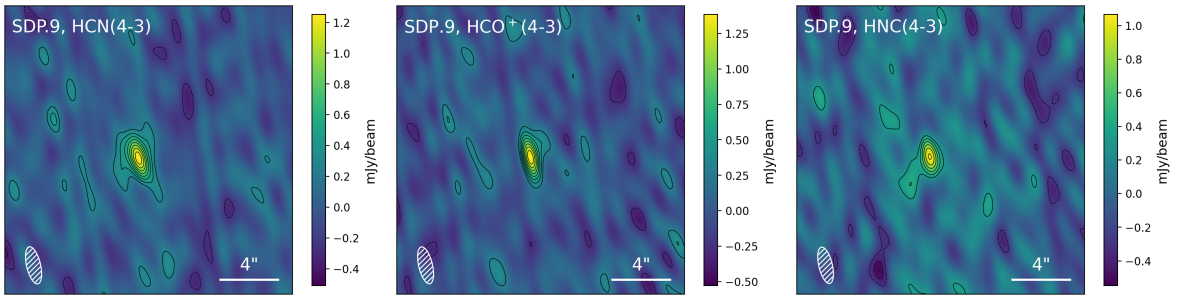

Fig. 2. NOEMA narrow-band images of the HCN/HCO^+/HNC lines for SDP.9, which is detected in all three transitions. For the remaining sources, see Appendix B. Contours start at $\pm 2\sigma$ and increase in steps of 2σ.

Table 2. Rest-frame frequencies and luminosities (in units of 10^8 K km s^{-1} pc^2) for HCN, HCO^+, and HNC lines in individual galaxies.

Line f_0 [GHz]	HCN(1–0) 88.632	HCN(3–2) 256.886	HCO^+(3–2) 267.558	HNC(3–2) 271.981	HCN(4–3) 354.505	HCO^+(4–3) 356.734	HNC(4–3) 362.630
SDP.9	380 ± 130^{O17}	164 ± 27^{O17}	85 ± 34^{O17}	99 ± 19^{O17}	84 ± 9	80 ± 13	83 ± 13
SDP.11	$\leq 540^{O17}$	170 ± 25^{O17}	73 ± 6^{O17}	$\leq 20^{O17}$	94 ± 24	≤ 54	≤ 35
G09v1.40	–	94 ± 19	113 ± 19	80 ± 18	–	–	–
SDP.17	–	–	–	–	126 ± 16	80 ± 16	125 ± 17
J1202	800 ± 400^{R22}	620 ± 90	600 ± 90	176 ± 90	230 ± 60	240 ± 60	≤ 120
G15v2.235	–	–	–	–	≤ 74	≤ 75	≤ 78
J0209	$\leq 1000^{R20}$	560 ± 70	310 ± 70	300 ± 50	960 ± 50^{NG}	480 ± 30^{NG}	570 ± 30^{NG}
G09v1.326	–	–	–	–	52 ± 13	61 ± 15	78 ± 13
SDP.130	$\leq 140^{R22}$	≤ 130	≤ 110	≤ 80	52 ± 23	≤ 45	31 ± 24
NAv1.195	–	–	–	–	180 ± 30	170 ± 20	≤ 290
$SDP.81^{R23}$	≤ 370	–	–	–	≤ 72	160 ± 43	≤ 71
G12v2.43	–	–	–	–	210 ± 15	146 ± 14	210 ± 15

Notes. The reported values are not corrected for lensing magnifications. The upper limits are given as 3σ. References: O17 – Oteo et al. (2017); R22 – Rybak et al. (2022); R23 – Rybak et al. (2023); NG – N. Geesink, MSc Thesis, Leiden 2025.

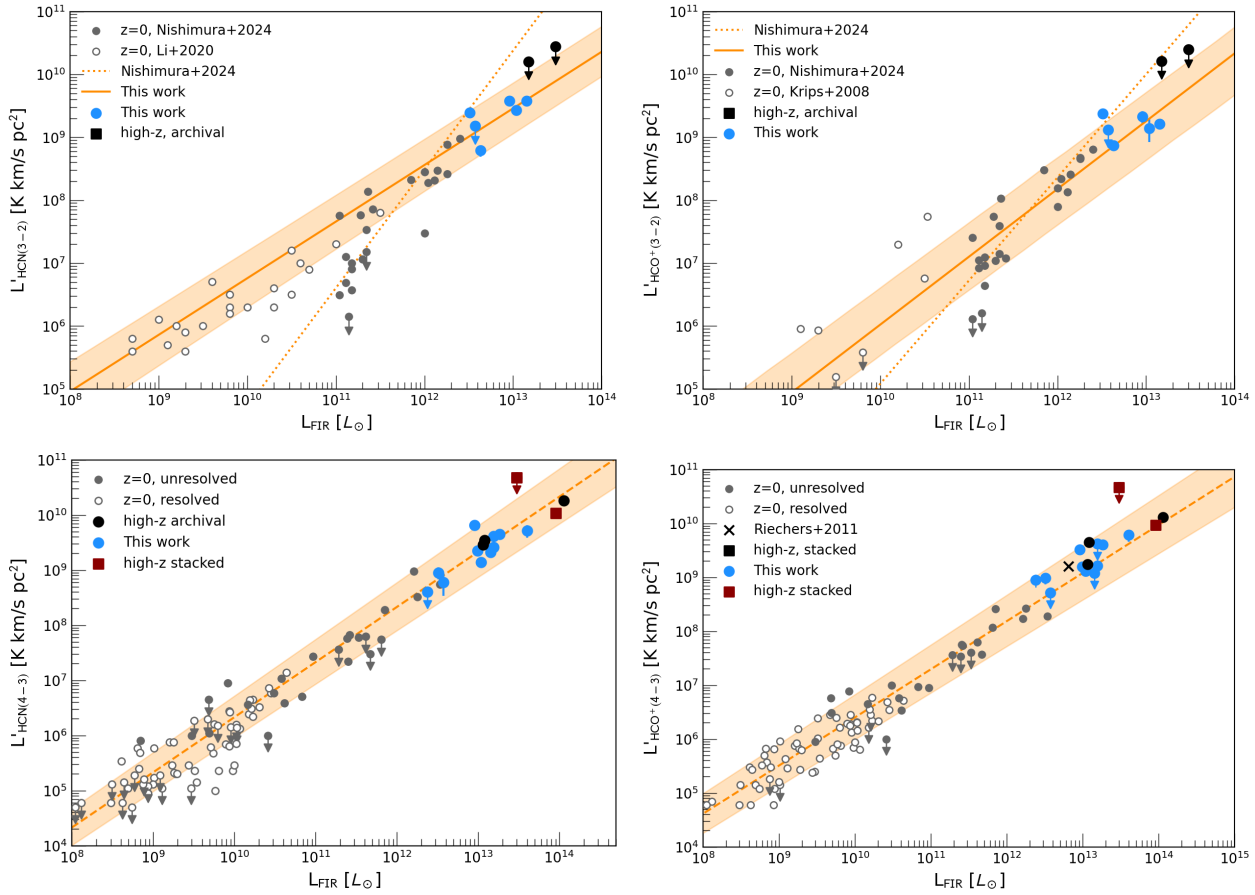

Fig. 3. Correlation between far-IR luminosity and HCN/HCO$^+$(3–2) and (4–3) luminosities. Solid/dashed orange lines indicate the empirical trends from this work and Zhang et al. (2014) with $\pm1\sigma$ scatter; dotted orange lines indicate the empirical trend from Nishimura et al. (2024). Individual data points show $z = 0$ galaxy-averaged (Greve et al. 2009; Papadopoulos et al. 2014; Zhang et al. 2014; Nishimura et al. 2024) and resolved observations (Tan et al. 2018), and high-z detections in individual galaxies (Riechers et al. 2011; Cañameras et al. 2021, black, solid) and this work (blue). We also show results from spectral stacks (Reuter et al. 2023; Hagimoto et al. 2023; red squares). Where appropriate, we corrected for the lensing magnification. We also plot error bars on high-z measurements; these are typically smaller than the symbol size.

bulk of molecular gas. Specifically, we fit a one-dimensional Gaussian profile to the slices of spectra within ±1000 km/s of the HCN, HCO$^+$, and HNC lines. Although some lines show more complex profiles (e.g. HNC(4–3) line in J1202, Fig. B.5), a one-dimensional Gaussian profile allows a direct comparison to the low-J CO linewidths reported in the literature. The measured linewidths are listed in Table 3.

Figure 5 compares the linewidths of HCN(3–2)/(4–3) and CO(1–0) lines. For J1202, we fit both the (3–2) and (4–3) lines; the HCN and HCO$^+$ linewidths are consistent, but HNC(4–3) is significantly narrower than HNC(3–2).

On average, we find that the linewidths of dense-gas tracers are consistent with those of CO(1−0) emission. Namely, the mean linewidth (FWHM) ratios are as follows: HCN/CO: 0.95 ± 0.20; HCO$^+$/CO: 0.70 ± 0.13; HNC/CO: 1.00 ± 0.27. However, several sources – particularly G09v1.40 and J1202 – show significant differences between different lines; we discuss them in detail in Section 4.7.1.

Table 3. HCN, HCO$^+$, and HNC FWHM linewidths for individual sources, inferred from one-dimensional Gaussian fits to the observed (i.e. not de-lensed) spectra.

Source	Lines	HCN [km/s]	HCO$^+$ [km/s]	HCN [km/s]
SDP.9	(3–2)	300 ± 40	320 ± 50	370 ± 60
G09.v140	(3–2)	390 ± 40	270 ± 20	670 ± 100
SDP.17	(4–3)	290 ± 40	170 ± 30	230 ± 40
J1202	(3–2)	470 ± 30	470 ± 60	300 ± 40
J1202	(4–3)	480 ± 50	400 ± 50	150 ± 40
J0209	(3–2)	310 ± 30	260 ± 30	300 ± 50
G09v1.326	(4–3)	260 ± 130	–	430 ± 160
SDP.130	(4–3)	810 ± 50	–	870 ± 220
NAv1.195	(4–3)	380 ± 70	210 ± 40	250 ± 70
G12v2.43	(4–3)	260 ± 20	190 ± 20	210 ± 10

4.3. HCN, HCO$^+$, and HNC line ratios

The ratios of HCN, HCO$^+$, and HNC line luminosities provide insights into the thermodynamics and energetics of high-density gas. In particular, HCN/HCO$^+$ enhancements have been proposed as an AGN signature (e.g. Kohno 2003; Graciá-Carpio et al. 2006; Krips et al. 2008; Privon et al. 2015; Izumi et al. 2016). However, as demonstrated by Viti (2017) and Privon et al. (2020), the HCN enhancements show rapid time evolution (on ≈1-Myr timescales) which decouples them from the AGN activity. Moreover, recent studies of nearby galaxies

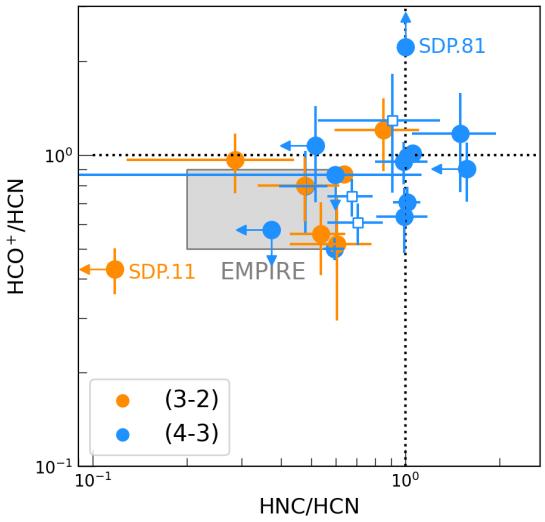

Fig. 4. HCO^+/HCN and HNC/CO luminosity ratios in our sample (solid circles). We also include data from Yang et al. (2023) for comparison (empty squares). The shaded regions indicate HCO^+/HCN and HNC/HNC ratios for the EMPIRE sample (Jiménez-Donaire et al. 2019). HCN is the brightest line in most of our targets. SDP.81 shows strong HCO^+ enhancement, potentially due to low metallicity (Rybak et al. 2023). The HCN(3–2) emission line in SDP.11 is unusually bright, potentially due to AGN-driven chemistry.

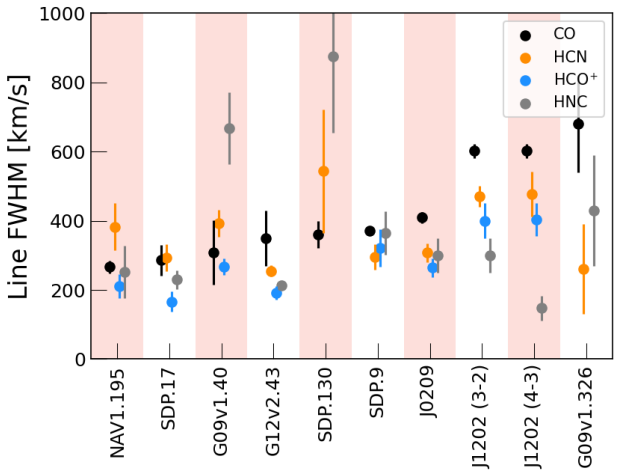

Fig. 5. Comparison of CO, HCN, HCO^+, and HNC linewidths in individual galaxies, ordered by increasing CO linewidth. The linewidths of different tracers are generally consistent within 1σ uncertainties. Note the large discrepancies between HCN/HCO^+ and HNC linewidths in G04v1.40 and J1202.

indicate that HCN/HCO^+ can be only used as a reliable AGN diagnostic at scales of ≤100 pc (Butterworth et al. 2025).

As is shown in Fig. 4, the HCO^+/HCN ratios in our sample are consistent with ≥1 with the exception of G12v2.43 and SDP.81. The elevated HCO^+ luminosity in these sources might be due to sub-solar metallicity or time-evolution effects (Rybak et al. 2023).

The HNC/HCN ratio has been proposed to be a sensitive diagnostic of the gas temperature. Specifically, while HCN and HNC form via the same pathways with a branching ratio of ≈1:1, their relative abundances are modified via the HNC + H → HCN + N reaction and HNC + O → NH + CO reations, with $\Delta T \approx 200$ K (e.g. Graninger et al. 2014; Jin et al. 2015; Hacar et al. 2020). As a result, the HNC/HCN ratio is predicted to decrease with increasing gas kinetic temperature (e.g. Hacar et al. 2020).

We find HNC/HCN ≤1 in all sources except G12v2.43 (HNC/HCN = 1.4 ± 0.2). Compared to the EMPIRE sample, our DSFGs have comparable HCO^+/HCN ratios, but have elevated HNC/HCN ratios. Using the Hacar et al. (2020) calibration $T_{\rm kin} = 10 \times [I_{\rm HCN}/I_{\rm HNC}]$, we find kinetic temperatures of 10−35 K, similar to those in the Orion Nuclear Cluster (Hacar et al. 2020).

4.4. Dense-gas tracer excitation

Measuring the HCN/HCO^+/HNC spectral line energy distribution (SLED) in DSFGs is necessary for a proper comparison of observations of different rotational transitions.

We observed four galaxies in multiple HCN transitions – J0209, J1202, SDP.9, and SDP.130. To anchor our SLEDs, we use ground-state observations from Oteo et al. (2017, SDP.9), Rybak et al. (2022, J1202, SDP.130) and Riechers et al. (in prep. J0209). For J0209, we include source-integrated HCN/HCO^+/HNC(4–3) fluxes from high-resolution ALMA observations (N. Geesink, MSc thesis 2025). Figure 6 shows the dense-gas SLEDs for our sample, compared to the HCN SLEDs in $z \sim 0$ galaxies from Israel (2023). While most SLEDs are consistent with being sub-thermalised ($r_{\rm j1} \leq 1$), J0209 and J1202 show superthermal ratios. This might be a result of non-thermal excitation by X-rays (e.g. Meijerink et al. 2007; Viti 2017; Privon et al. 2020) or infrared pumping (e.g. Sakamoto et al. 2010; Rangwala et al. 2011; Martín et al. 2021), or optical depth effects (e.g. if the ground-state transition has lower optical depth than the upper-state ones).

Combining the detections and upper limits on $r_{\rm j1}$ in our sample, we calculated the mean excitation ratios r_{31} and r_{41}, assuming all high-z DSFGs share a common $r_{\rm j1}$. The inferred mean $r_{\rm j1}$ are listed in Table 4.

The inferred median $r_{\rm j1}$ are systematically higher than in most $z \sim 0$ (ultra)luminous infrared galaxies (ULIRGS) from Israel (2023) (median $r_{31} = 0.33 \pm 0.18$, $r_{41} = 0.19 \pm 0.15$), although the low-redshift and high-redshift values are consistent within 1σ. However, some local sources have HCN excitation similar to (e.g. NGC 1068) or even higher (e.g. NGC 253, NGC 6240) than our high-redshift targets.

Finally, we tested whether $r_{\rm j1}$ excitation ratio depends on the FIR luminosity, combining our data with observations of nearby galaxies (Li et al. 2020; Israel 2023). We find that the data is consistent with a null hypothesis of a constant $r_{\rm j1}$. The lack of correlation of HCN excitation with $L_{\rm FIR}$ mirrors the results of Li et al. (2020), who report no significant correlation of HCN(3–2)/HCN(1–0) luminosity with $L_{\rm FIR}$ over $L_{\rm FIR} = 10^8$–10^{12} $L_\odot$.

In this analysis, we remain agnostic about the physical mechanism driving the dense-gas excitation (e.g. heating by turbulence, cosmic rays or X-rays; mid-infrared pumping); our objective was simply to derive the median excitation coefficients to obtain the HCN(1–0) luminosities. We will explore dense-gas thermodynamics in future work.

4.5. Star-forming efficiencies and dense-gas fractions in DSFGs

Armed with the constraints on the HCN excitation, we assessed the dense-gas star-forming efficiency $\rm SFE_{dense} = M_{dense}/SFR$ and dense-gas fractions for our sample. We first calculated $\rm SFE_{dense}$,

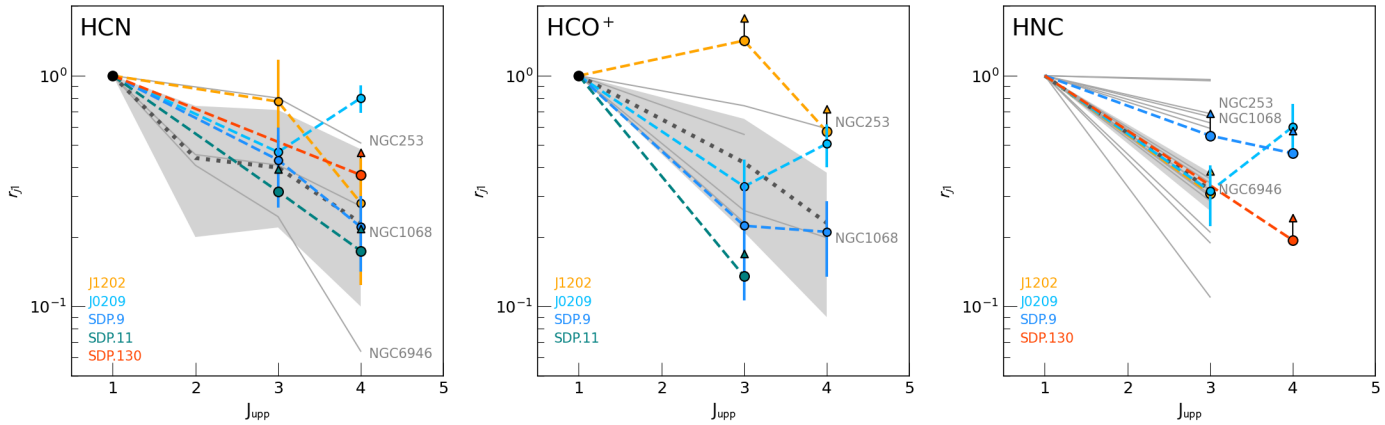

Fig. 6. Excitation coefficients of HCN, HCO^+, and HNC in DSFGs from our sample (coloured), normalised to the (1–0) transition and compared to $z \sim 0$ galaxies from the Israel (2023) compilation (grey). The arrows indicate the 3σ upper/lower limits. For comparison, we highlight SLEDs for nearby (U)LIRGs NGC 253, NGC 1068, and NGC 6946. In J0209 and J1202, the HCN and HCO^+ SLEDs appear to be superthermalised. The sparseness of the HNC plot reflects the lack of detections at $z \approx 0$.

Table 4. Median excitation ratios for HCN, HCO^+, and HNC lines, derived from data in Fig. 6.

Species	This work		Israel (2023)	
	r_{31}	r_{41}	r_{31}	r_{41}
HCN	$0.59^{+0.17}_{-0.14}$	$0.41^{+0.04}_{-0.04}$	$0.33^{+0.18}_{-0.18}$	$0.19^{+0.15}_{-0.15}$
HCO^+	$0.36^{+0.10}_{-0.10}$	$0.27^{+0.05}_{-0.05}$	$0.42^{+0.23}_{-0.21}$	$0.22^{+0.16}_{-0.13}$
HNC	≥ 0.34	≥ 0.22	$0.33^{+0.34}_{-0.09}$	–

Notes. The listed uncertainties correspond to the 16th and 84th percentile, respectively.

assuming it is directly proportional to the ratio of HCN(1–0) luminosity and obscured star formation, $\mathrm{SFR} = 1.71{\times}10^{-10}{\times}L_{\mathrm{FIR}}$ for the Salpeter stellar initial mass function.

We derived the dense-gas mass M_{dense} for each galaxy as:

$$M_{\mathrm{dense}} = r_{\mathrm{j1}}\alpha_{\mathrm{HCN(1-0)}}L'_{\mathrm{HCN(j-j-1)}}, \quad (5)$$

where and α_{HCN} is the conversion factor between HCN(1–0) luminosity and the dense-gas mass.

Specifically, we corrected our HCN(4–3) and HCN(3–2) observations using r_{41} and r_{31} factors derived in Section 4.4. For galaxies where both HCN(3–2) and HCN(4–3) are detected, we list values inferred from the lower-J line. For α_{HCN}, we assumed the canonical value of $10\,M_\odot(\mathrm{K\,km\,s^{-1}})^{-1}$ (Gao & Solomon 2004b); see Section 4.7 for a more detailed discussion of this choice.

As is shown in Fig. 7, almost all of our data points fall below the mean HCN(1–0)/FIR trend in nearby galaxies from Jiménez-Donaire et al. (2019): $\mathrm{HCN(1–0)/FIR} = 10^{-3}$, with a 1σ spread of 0.37 dex. Our sample has a median HCN(1–0)/FIR ratio of $4^{+11}_{-1} \times 10^{-4}$, approximately 1σ below the median for nearby galaxies ($1^{+10}_{-5} \times 10^{-3}$, Jiménez-Donaire et al. 2019). The joint probability of our HCN/FIR ratios being consistent with the Jiménez-Donaire et al. (2019) value is $p \approx 10^{-3}$; i.e. DSFGs as a population have significantly lower HCN/FIR ratios. As there are no $z \approx 0$ galaxies with FIR luminosities comparable to our sample, we cannot determine whether this turnover in HCN/FIR ratio (i.e. a deviation from a linear HCN–FIR correlation) is related to the higher redshift or a higher FIR luminosity of DSFGs. Turnover in HCN/FIR in intensely star-forming galaxies was predicted by theoretical models of Krumholz & Thompson (2007), where it is a consequence of median density exceeding the critical density for HCN emission.

Figure 8 shows the inferred HCN(1–0)/FIR (a proxy for dense-gas depletion time, $\tau_{\mathrm{dense}} = M_{\mathrm{dense}}/\mathrm{SFR}$) and HCN(1–0)/CO(1–0) (a proxy f_{dense}). For $z = 0$ galaxies, we plot the galaxy-integrated observations of Gao & Solomon (2004a), Graciá-Carpio et al. (2008), Krips et al. (2008), García-Burillo et al. (2012), Privon et al. (2015).

The HCN(1–0)/CO(1–0) luminosity ratios range between 0.01 (SDP.9) and 0.36 (SDP.11), with a median of $0.08^{+0.12}_{-0.03}$; about half of our sample has $\mathrm{HCN/CO} \leq 0.05$. While the HCN/CO ratios can be affected by differential magnification (Section 4.7.2), the wide spread of values likely refers real physical differences between individual sources. We did not find a significant correlation between HCN/FIR and HCN/CO.

Assuming that α_{HCN} does not change between $z = 0$ and $z = 2.5$, this implies a significantly elevated $\mathrm{SFE_{dense}}$. We estimated the dense-gas and total molecular gas mass – and the corresponding depletion timescales – using conversion factors $\alpha_{\mathrm{HCN}} = 10$ and $\alpha_{\mathrm{CO}} = 1$ (Table 5). Our choice of $\alpha_{\mathrm{CO}} = 1$ was motivated by kinematic constraints on gas masses in DSFGs (e.g. Calistro Rivera et al. 2018; Frias Castillo et al. 2022; Amvrosiadis et al. 2025), although higher values have been proposed for some systems (e.g. Dunne et al. 2022; Harrington et al. 2021).

We find a median dense-gas fraction $f_{\mathrm{dense}} = 0.8^{+1.2}_{-0.3}$ and a median dense-gas depletion timescale of $\tau_{\mathrm{dense}} = 24^{+22}_{-12}$ Myr. This is significantly shorter than the typical $\tau_{\mathrm{dense}} \simeq 60$ Myr in nearby spiral galaxies from the EMPIRE survey (Jiménez-Donaire et al. 2019). The increase in SFE would be further reinforced if DSFGs have lower α_{HCN} than $z \approx 0$ spiral galaxies (e.g. Graciá-Carpio et al. 2008; Jones et al. 2023; Vollmer et al. 2025; see Section 4.7.3 for more detail).

How do dense-gas depletion timescales compare to the depletion timescales for the total molecular gas? Figure 9 compares the depletion times for the total molecular gas (traced by CO) and dense gas (traced by HCN). Assuming $\alpha_{\mathrm{CO}} = 1\,M_\odot(\mathrm{K\,km\,s^{-1}\,pc^2})^{-1}$, the molecular gas depletion times τ_{mol} range between 11 Myr (G12v2.43) and 110 Myr (SDP.9). The dense-gas depletion timescales τ_{dense} range between 10 and 30 Myr, with a mean of 18 ± 5 Myr. In almost all cases, τ_{dense} is systematically lower than τ_{mol}. This discrepancy would increase

Table 5. Dense-gas masses, fractions, and dense-gas and molecular-gas depletion timescales for individual galaxies.

Source	Line	$M_{\rm dense}$ [$10^9\,M_\odot$]	$f_{\rm dense}$	$\tau_{\rm dense}$ [Myr]	$\tau_{\rm mol}$ [Myr]
SDP.9	(3–2)	66 ± 4	0.08 ± 0.01	35 ± 2	12 ± 3
SDP.11	(3–2)	92 ± 6	3.19 ± 0.19	38 ± 2	12 ± 2
G09v1.40	(3–2)	15 ± 1	0.76 ± 0.06	20 ± 2	27 ± 12
SDP.17	(4–3)	44 ± 3	0.82 ± 0.06	16 ± 1	20 ± 7
J1202	(3–2)	60 ± 4	1.06 ± 0.07	109 ± 7	103 ± 36
G15v2.235	(4–3)	≤ 70	≤ 0.26	≤ 26	91 ± 25
J0209	(3–2)	93 ± 5	1.63 ± 0.09	60 ± 3	37 ± 5
G09v1.326	(4–3)	88 ± 13	0.27 ± 0.04	13 ± 2	48 ± 13
SDP.130	(4–3)	10 ± 3	0.35 ± 0.09	16 ± 4	46 ± 8
NAv1.195	(4–3)	76 ± 7	0.54 ± 0.05	24 ± 2	44 ± 20
SDP.81	(4–3)	≤ 7	≤ 0.23	≤ 17	73 ± 15
G12v2.43	(4–3)	38 ± 2	2.28 ± 0.10	23 ± 1	10 ± 2

Notes. The second column indicates the line used to derive dense-gas mass. Excitation coefficients adopted from Table 4. We assume $\alpha_{\rm CO} = 1$ and $\alpha_{\rm HCN} = 10$.

further for $\alpha_{\rm CO} \geq 1$ or $\alpha_{\rm HCN} \leq 10\,M_\odot(\mathrm{K\,km\,s^{-1}\,pc^2})^{-1}$. In case of G12v2.43 and SDP.11, $\tau_{\rm dense} \geq \tau_{\rm mol}$, which is clearly unphysical. This is a clear indication that our assumption on $\alpha_{\rm CO} = 1$ and $\alpha_{\rm HCN} = 10$ are not applicable to all DSFGs.

We can get additional insights into the process of star-formation by considering the star-forming efficiency per free-fall time (e.g. Krumholz & McKee 2005). The free-fall timescale of a self-gravitating cloud with a density ρ is $t_{\rm ff} = \sqrt{3\pi/(32G\rho)}$, where G is the gravitational constant and ρ the mean gas density, $\rho = m_u n$. Setting $n = 3 \times 10^4\,\mathrm{cm^{-3}}$, we obtain $t_{\rm ff} = 0.25$ Myr which is comparable to the expected formation timescale for O-type stars (≈0.5 Myr, e.g. Sabatini et al. 2021). The corresponding dense-gas star-forming efficiency per free-fall time $\epsilon_{\rm ff} = t_{\rm dep}/t_{\rm ff}$ (Krumholz & McKee 2005) is then $1.3 \pm 0.4\%$, compared to ≈0.4% for nearby galaxies (Jiménez-Donaire et al. 2019; Salim et al. 2020). The higher value of $\epsilon_{\rm ff}$ in DSFGs is comparable with estimates for present-day (U)LIRGs (1.4%, Usero et al. 2015).

In reality, dense cores have a complex three-dimensional geometry and will be subject to various internal processes. For a more realistic comparison, we use the results of hydrodynamical simulations of individual star-forming clouds by Onus et al. (2018). Using chemical and radiative transfer modelling, and allowing for an environment-dependent $\alpha_{\rm HCN}$, Onus et al. (2018) derived an empirical scaling relation between the FIR/HCN(1–0) luminosity:

$$\mathrm{SFR} = 2.6 \times 10^{-7} \left(\frac{\epsilon_{\rm ff}}{0.01}\right)^{0.9} L'_{\rm HCN(1-0)}, \tag{6}$$

which yields $\epsilon_{\rm ff} = 2.3 \pm 0.6\%$, similar to $1.3 \pm 0.4\%$ derived for a self-gravitating cloud.

4.6. Redshift evolution of dense-gas mass density

We now use our high-redshift observations to estimate the evolution of dense-gas mass density $\rho_{\rm dense}$, between the redshift range probed by our sample ($z = 1.5$–3.2) and the present-day. This "Madau-Dickinson" plot complements the evolution of the cosmic star-formation density (e.g. Madau & Dickinson 2014) and molecular gas density (e.g. Riechers et al. 2019; Tacconi et al. 2020; Walter et al. 2020). Such trends can serve as a powerful benchmark for the latest cosmological simulations that now directly include cold, dense gas (e.g. COLIBRE, Schaye et al. 2025).

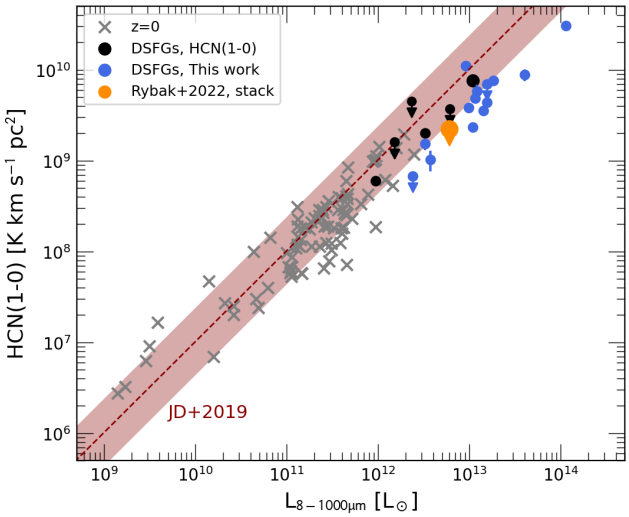

Fig. 7. HCN(1–0) vs FIR luminosity (8–1000 μm) for our sample (blue), compared to other high-redshift (black) and selected low-redshift (grey) measurements for entire galaxies (Gao & Solomon 2004a; Graciá-Carpio et al. 2008; Krips et al. 2008; García-Burillo et al. 2012; Privon et al. 2015), and the empirical linear trend from Jiménez-Donaire et al. (2019, red). Our measurements fall systematically below the linear HCN-FIR correlation.

We make the following assumptions:

(i) HCN(1–0) luminosity is directly proportional to the dense-gas mass, $M_{\rm dense} = \alpha_{\rm HCN} \times L'_{\rm HCN(1-0)}$.
(ii) A universal $\alpha_{\rm HCN}$ that does not depend on galaxy properties or redshift.
(iii) The HCN excitation ($r_{\rm j1}$) does not depend on galaxy properties, but varies with redshift.
(iv) The $L'_{\rm HCN(1-0)}/L_{\rm FIR}$ ratio (i.e. dense-gas star-forming efficiency) varies with redshift, but not with galaxy properties.

The cosmic dense-gas mass density then can be expressed as:

$$\phi_{\rm dense}(z) = \alpha_{\rm HCN} \frac{L'_{\rm HCN(1-0)}}{L_{\rm FIR}}\bigg|_z \int \phi(L_{\rm FIR}, z)\,\mathrm{d}L_{\rm FIR}. \tag{7}$$

The assumptions above are, by necessity, simplifying. However, there is a strong case for a redshift evolution of dense-gas excitation and dense-gas star-forming efficiency. This is because the morphology and properties of "typical" star-forming galaxies, as well as (U)LIRGS, change dramatically between present day and the Cosmic Noon.

First, high-redshift galaxies have both higher star-formation rates and star-forming efficiency, even at the same stellar mass as $z \approx 0$ ones (e.g. Tacconi et al. 2020). Second, high-redshift DSFGs are morphologically distinct from present-day ULIRGs with comparable $L_{\rm FIR}$: while star formation in ULIRGs is typically concentrated into a very compact region (just a few hundred parsecs across, e.g. Lutz et al. 2016; Barcos-Muñoz et al. 2017), in high-redshift galaxies, it is spread over a region few kiloparsecs across (e.g. Hodge et al. 2016; Gullberg et al. 2019). Third, DSFGs have significantly higher gas densities, far-UV irradiation (e.g. Wardlow et al. 2017; Rybak et al. 2019), and are potentially more turbulent (e.g. Dessauges-Zavadsky et al. 2019; Harrington et al. 2021). Finally, as we will discuss in Appendix C, high-redshift DSFGs might have a top-heavy

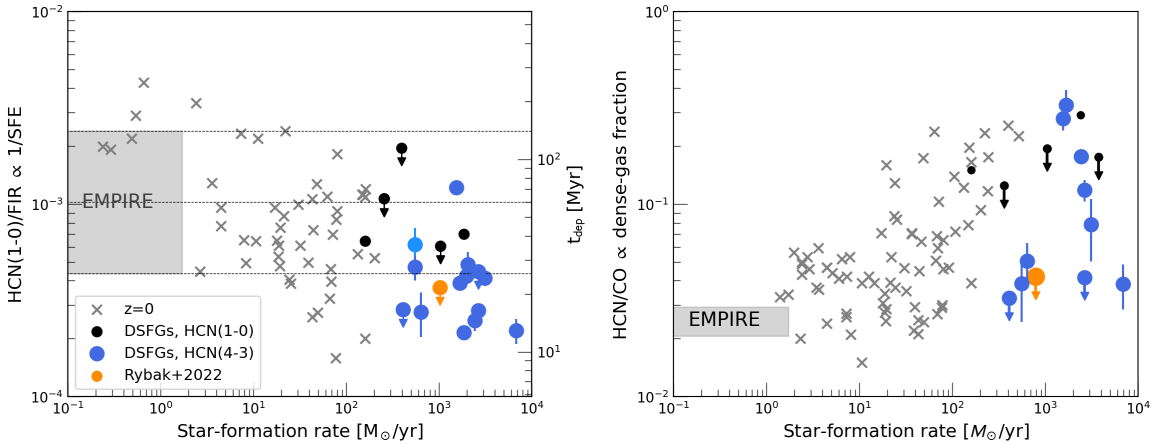

Fig. 8. Left: Ratio of HCN(1–0) and FIR luminosities (a proxy for star-forming efficiency) as a function of star-formation rate. The dotted lines indicate the mean and 1σ scatter for local galaxies from the EMPIRE sample (Jiménez-Donaire et al. 2019). We infer HCN(1–0) luminosities for our DSFGs using the following excitation coefficients: $r_{31} = 0.41$ and $r_{41} = 0.59$. Right: Ratio of HCN(1–0) and CO(1–0) luminosities (a proxy for the dense-gas fraction). The inferred HCN/CO ratios span ≈1 dex, suggesting that dense-gas fraction in high-z DSFGs vary significantly source-to-source.

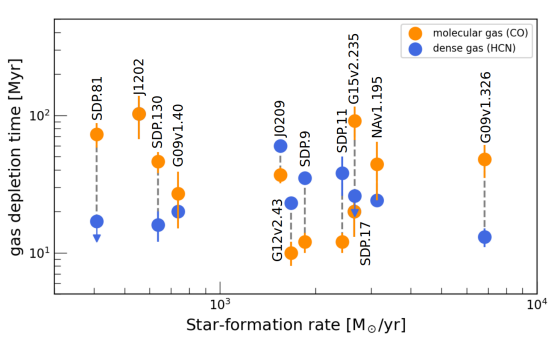

Fig. 9. Depletion timescales for the total molecular gas $\tau_{\rm mol}$ (orange, based on CO(1–0)) and dense gas $\tau_{\rm dense}$ (blue, based on HCN) for individual DSFGs from our sample. The gas masses are derived using $\alpha_{\rm CO} = 1$ and $\alpha_{\rm HCN} = 10$. In several galaxies, $\tau_{\rm dense} \geq \tau_{\rm mol}$; this indicates that $\alpha_{\rm CO}$ and/or $\alpha_{\rm HCN}$ deviate from the assumed values. The median dense-gas depletion timescale is 24 Myr.

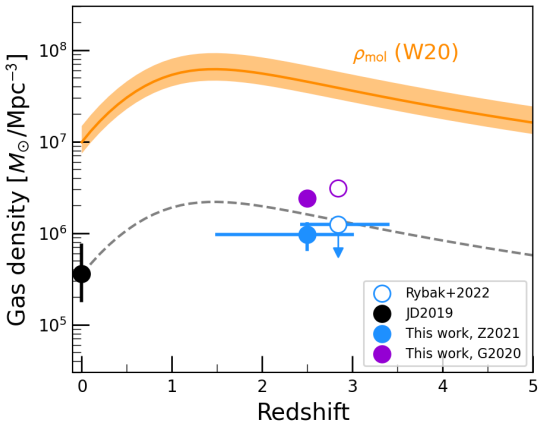

Fig. 10. Redshift evolution of dense-gas mass density between the present-day (black point). The blue and purple points show dense-gas mass density inferred using the far-IR LFs from Zavala et al. (2021, blue) and Gruppioni et al. (2020, purple), respectively. The $z \approx 0$ point (black) is inferred using HCN/FIR ratio from Jiménez-Donaire et al. (2019). We also show the upper limit from Rybak et al. (2022). Orange line points shows the evolution of total molecular gas density $\rho_{\rm mol}$ from Walter et al. (2020, orange solid line). Grey dashed line shows the Walter et al. (2020) trend normalised to match $\rho_{\rm dense}$ at $z = 0$. The $\rho_{\rm dense}$ evolution is consistent with the redshift evolution of $\rho_{\rm mol}$ with a constant dense-gas fraction of ≈3.5%.

stellar IMF. We discuss the potential impact of all these factors below.

We match our galaxies to the far-infrared luminosity functions (FIR LFs), rather than the stellar mass functions[9]. As our fiducial model, we adopt FIR LFs derived by Casey et al. (2018) and Zavala et al. (2021). For comparison, we repeat our calculations using FIR LFs of Gruppioni et al. (2013) for $z = 0$ and Gruppioni et al. (2020) for high redshift; while the latter overpredicts the star-formation rate density at $z \geq 4$ (e.g. Zavala et al. 2021; van der Vlugt et al. 2022), it still provides a good fit to the observational data over the redshift range considered here.

Figure 10 shows the resulting constraints on the redshift evolution of $\rho_{\rm dense}$. For the Casey et al. (2018) and Zavala et al. (2021) LFs, $\rho_{\rm dense}$ increases from $3.6^{+3.4}_{-1.9} \times 10^5\ M_\odot\,{\rm Mpc}^{-3}$ at $z = 0$ to $(9.6 \pm 3) \times 10^6\ M_\odot\,{\rm Mpc}^{-3}$ at $z = 2.5$. This corresponds to an increase by factor of ≈3, but the $z = 0$ and $z = 2.5$ values are essentially consistent within 1.3σ, due to the considerable uncertainties on both measurements. For the Gruppioni et al. LFs, $\rho_{\rm dense}$ increases from $(3.6^{+3.4}_{-1.8}) \times 10^5\ M_\odot\,{\rm Mpc}^{-3}$ at $z = 0$ to $(24 \pm 8) \times 10^5\ M_\odot\,{\rm Mpc}^{-3}$ at $z = 2.5$. This translates to an increase by a factor of ≈7 (1.8σ significance). In summary, we see a tentative increase in $\rho_{\rm dense}$ towards high redshift.

We complement our constraint on $\rho_{\rm dense}$ at $z = 2.5$ by the upper limit on HCN/FIR ratio from Rybak et al. (2022) ($\geq 3.6 \times 10^{-4}$), which was derived directly from HCN(1–0) observations and is not affected by uncertainties on $r_{\rm j1}$. The Rybak et al. (2022) upper limit puts a nominally stronger constraint on $\rho_{\rm dense}$ at $z = 2.5$–3.5 (increase by a factor of $\leq$3.0 compared to $z = 0$), but is derived from a smaller sample of galaxies.

The tentative increase in $\rho_{\rm dense}$ is qualitatively in line with the higher molecular gas mass density $\rho_{\rm mol}$ at high redshift (e.g. Tacconi et al. 2020; Walter et al. 2020). For a more quantitative comparison, Fig. 10 shows the constraints on the total

[9] While the stellar mass functions at high redshift are better observationally constrained, the stellar masses of dusty DSFGs are highly uncertain. Moreover, for lensed sources, the light from the background galaxy is blended with that from the foreground lens.

molecular gas mass from the Walter et al. (2020) compilation (orange), and the Walter et al., trend normalised to $\rho_{\rm dense}$ at $z = 0$ (grey line). Our constraints on the redshift evolution of dense gas are consistent with the $\rho_{\rm mol}$ trend, with a mean dense-gas fraction of ≈3.5%. This fraction is considerably lower than the dense-gas fractions derived for individual DSFGs (Table 5); however, the latter might suffer from a considerable uncertainty due to conversion factors or differential magnification. The constant dense-gas fraction indicate that the increase of SFR density at high redshift is driven by enhanced star-forming efficiencies rather than increased availability of dense gas – a direct.

4.7. Systematic uncertainties

4.7.1. Spatial offsets and differences in line profiles

Throughout this study, given the low angular (and spectral) resolution of our data, we assume that HCN, HCO^+, and HNC emission trace the same gas. We now examine this assumption by looking for: (1) differences between the HCN/HCO^+/HNC line profiles; (2) spatial offsets in moment-0 maps.

As is shown in Fig. 5, line profiles – parametrised by their Gaussian FWHM – are generally consistent within 2σ uncertainties. A similar correspondence was found for $J_{\rm upp} = 4, 5$ lines in three galaxies high-z by Cañameras et al. (2021). However, noticeable differences are seen in several sources with high S/N: G09v1.40, J0209, and J1202. First, in G09v1.40, the HNC(3–2) line appears to be double-peaked, with a prominent blueshifted emission offset by 350 ± 50 km/s from the systemic redshift. In contrast, the HCN(3–2) and HCO^+(3–2) lines are consistent with a Gaussian profile. We note that G09v1.40 has a massive molecular outflow, detected in the CH^+ (Falgarone et al. 2017) and OH^+ emission with an outflow velocity of ≈250 km/s (Butler et al. 2021). The HNC emission might be associated with this molecular outflow.

In J0209, the HCN, HCO^+, and HNC lines have comparable linewidths, but are systematically (≈30%) narrower than the CO emission. This is consistent with a picture where the bulk of low-J CO emission arises from extended gas reservoir (e.g. König et al. 2018; Rybak et al. 2025), as has been confirmed by high-resolution ALMA observations (N. Geesink, MSc thesis).

Finally, in J1202, the HNC(3–2) and HCN(4–3) are significantly narrower than the corresponding HCN and HCO^+ transitions. Compared to the HCN and HCO^+(4–3) lines, the peak of HNC emission is shifted 160 ± 15 km/s towards red, with absorption in the blue wing of the line – a P-Cygni profile, indicative of outflowing gas. We therefore hypothesise that in G09v1.40 and J1202, a significant fraction of the HNC (but not HNC or HCO^+) emission arises from a molecular outflow.

Looking at the moment-0 maps, the dust, HCN, HCO^+, and HNC emission can be considered co-spatial for almost all the sources – with the exception of NAv1.195. As is shown in Fig. 11, in this source, the dust (peak S/N ≃ 9) and HCN(4–3) surface brightness distribution (peak S/N ≃ 6) peak the same position. However, HCO^+(4–3) (peak S/N ≈ 5) is offset to the south by ≈2.5″. This offset is comparable to the synthesised beam FWHM (2.8″ × 1.6″) and thus likely to be physical. The HCN/HCO^+ enhancement in the north of the source could be caused, for example, by a buried AGN (see Section 4.3).

4.7.2. Differential magnification

In gravitational lensing, different spatial distributions of different tracers will cause them to be magnified by a different factor – the so-called differential magnification (e.g. Serjeant 2012).

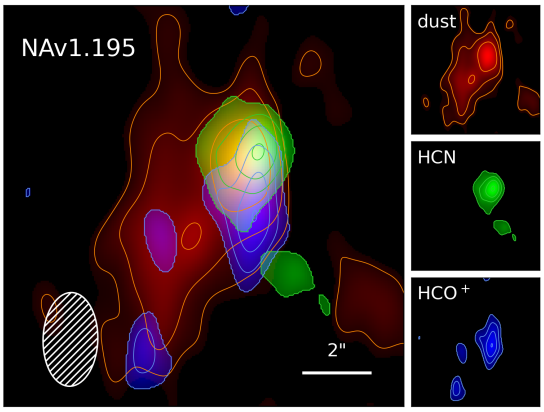

Fig. 11. Spatial offsets between HCN (green) HCO^+ (blue) and dust (red) emission in NAv1.195. The contours are drawn at ±(2, 4, 6, …)σ for the continuum, and ±(2, 3, 4, …)σ for the lines. The HCO^+(4–3) emission peaks ≈2.5″ to the south of HCN and dust continuum. These offsets suggest that different dense-gas tracers do not necessarily trace the same gas.

Namely, if the CO(1–0) emission is much more extended than HCN or FIR continuum and thus extends to low-magnification regions, the total magnification factor for CO will be smaller than for the more compact HCN or FIR. This would artificially inflate the observed HCN/CO ratios, while HCN/FIR will be less affected, as dense gas and obscured star-formation are likely almost co-spatial (and we can thus apply magnifications derived for FIR continuum to dense-gas tracers).

For example, in SDP.81, the difference between FIR and CO(3–2) magnifications is ≤10% (Rybak et al. 2020). Similarly, Cañameras et al. (2018) found that CO and FIR magnifications differ by ≤20% in a sample of nine lensed DSFGs from the *Planck* sample. In extreme case of SDP.9 – which, as a very compact source, is particularly sensitive to differential magnification – Massardi et al. (2018) find a 50% difference between the magnification of the FIR continuum and the stellar component. Typical differences in CO and FIR continuum magnifications are therefore likely ≤50%. Overall, the high HCN/CO values are likely physical, and not driven by the differential magnification.

4.7.3. The HCN-to-dense-gas conversion factor

The most significant systematic uncertainty for the interpretation of our results is the conversion factor between the HCN luminosity and dense-gas mass (Eq. 5). In particular, there is a considerable uncertainty regarding the 'effective' gas density traced by the HCN(1–0) emission. Specifically, spatially resolved studies of Galactic molecular clouds have shown that on (sub-)parsec scales, a significant fraction of HCN(1–0) emission is associated with densities as low as 10^3 cm^{-3} (Kauffmann et al. 2017; Evans et al. 2020). Similarly, magneto-hydrodynamic simulations of individual molecular clouds indicate that HCN(1–0) traces gas with a mean density of ≈3 × 10^3 cm^{-3} (Jones et al. 2023). However, recent observations by Jiménez-Donaire et al. (2023) have shown that in nearby galaxies, HCN(1–0) directly correlates with N_2H^+ emission on kiloparsec scales. As N_2H^+ is considered an unambiguous tracer of dense gas in molecular clouds (N_2H^+ traces gas with characteristic density ≈4 × 10^3 cm^{-3}, Kauffmann et al. 2017), this implies that on galactic scales, HCN remains a reliable tracer dense gas.

Gao & Solomon (2004b) estimated $\alpha_{\rm HCN} = 10\,M_\odot/(\rm K\,km\,s^{-1}\,pc^2)$ using two approaches: (1) large velocity-gradient modelling; and (2) considering optically thick emission from a virialised cloud[10]. However, this conversion factor is far from universal. As already noted by Gao & Solomon (2004b), $\alpha_{\rm HCN}$ has to differ significantly between individual galaxies. For example, many $z \approx 0$ ULIRGs have HCN(1–0)/CO(1–0) luminosity ratios ≥0.1 (see Fig. 8); assuming $\alpha_{\rm HCN} = 10$ and $\alpha_{\rm CO} = 0.8$ would yield dense-gas fractions in the excess of 100% – a clearly unphysical result. This was confirmed by Graciá-Carpio et al. (2008) who found that $\alpha_{\rm HCN}$ decreases by a factor of ≈2.5 over the $L_{\rm FIR} = 10^{11}$–$10^{12}\,L_\odot$ range, based on LVG modelling of HCN/HCO$^+$ (1–0) and (3–2) lines. Finally, spatially resolved ALMA observations of HCN and CO emission in J0209 imply $\alpha_{\rm HCN} \leq 2$ (Rybak, Geesink et al., in prep.).

Conversely, several studies of nearby galaxies report $\alpha_{\rm HCN} \geq 10$. For example, Papadopoulos et al. (2014) derived $\alpha_{\rm HCN} = 20$–60 for Arp 193 and NGC 6240; for the latter galaxy, Tunnard et al. (2015) report $\alpha_{\rm HCN} = 32^{+89}_{-13}$. More recently, very elevated $\alpha_{\rm HCN} \approx 100$ has been reported for individual clouds in the Milky Way (Dame & Lada 2023) and Andromeda (Forbrich et al. 2023). However, as these would imply $f_{\rm dense} \geq 100\%$, these are clearly not applicable to all DSFGs, although the actual $\alpha_{\rm HCN}$ value might vary significantly between individual sources.

Simulations of individual star-forming clouds and galaxies also support $\alpha_{\rm HCN} \leq 10$. On cloud scales, Onus et al. (2018) found $\alpha_{\rm HCN} = 16 \pm 4$; while Jones et al. (2023) found $\alpha_{\rm HCN} = 6.8 \pm 3.8$ in simulations of colliding clouds, with high-velocity collisions showing $\alpha_{\rm HCN} \leq 3$. On galactic scales, simulations by Vollmer et al. (2025) predict a mean $\alpha_{\rm HCN} = 11 \pm 4$ and 12 ± 7 for high-redshift starburst and main-sequence galaxies, respectively, with $\alpha_{\rm HCN} \approx 6$ for $z = 0$–0.5 LIRGs.

A variable $\alpha_{\rm HCN}$ which decreases at high SFR would in fact reinforce our main findings. Specifically, our inferred $M_{\rm dense} = \alpha_{\rm HCN} L'_{\rm HCN(1-0)}$ would become even smaller, further increasing the dense-gas star-forming efficiency. In other words, in the HCN/FIR – SFR plane (Fig. 8, left), our datapoints would shift downwards, towards very short depletion times (≤10 Myr). Similarly, in the HCN/CO – SFR plane (Fig. 8, right), our data points would shift downwards, towards even lower dense-gas fraction.

Finally, it is possible that $\alpha_{\rm CO}$ is ≥1 in (some) high-redshift DSFGs (e.g. Harrington et al. 2021). In such a case, the inferred dense-gas fractions would decrease even further. On the other hand, the inferred $\tau_{\rm dense}$ – which is independent of $L'_{\rm CO(1-0)}$ – would remain unchanged.

5. Conclusions

We have presented results of the NOEMA and ALMA survey of dense-gas tracers – HCN, HCO$^+$, and HNC – in 11 $z = 1.6$–3.1 DSFGs. This is the largest study of dense-gas tracers in $z \geq 1$ galaxies to date. Our main results are:

- We detect dense-gas tracers in 10 out of 11 galaxies. In total, we detect 34 transitions of HCN, HCO$^+$, and HNC, increasing the number of $z \geq 1$ detections by more than a factor of four. Only one galaxy (G15v2.235) is not detected in any spectral line. Additionally, we also detect several transitions of ^{13}CO, C^{18}O, and CN.
- The linewidths of HCN, HCO$^+$, and HNC lines are generally consistent within 1σ uncertainty. However, in G09v1.40 and J1202, the HNC lines show structures indicative of molecular outflows. In one source – NAv1.195 – the HCN and HCO$^+$ emission appear to be spatially offset from each other.
- We derive the excitation coefficients for the HCN, HCO$^+$, and HNC $J_{\rm upp} = 3$ and 4 lines, and find that DSFGs have more excited dense-gas ladders than $z \approx 0$ (U)LIRGs.
- High-redshift DSFGs have systematically lower HCN(1–0)/FIR ratios compared to present-day star-forming galaxies. This trend agrees qualitatively with a break in the HCN-FIR correlation predicted by some theoretical models (e.g. Krumholz & Thompson 2007).
- Assuming $\alpha_{\rm HCN} = 10$ from Gao & Solomon (2004b), we find a median dense-gas depletion timescale of ≈24 Myr. These results indicate that high-redshift DSFGs had higher star-forming efficiency than present-day galaxies.
- High-redshift DSFGs have a wide range of dense-gas fractions, with HCN/CO ratios ranging from ≈0.01 to ≈0.15. This likely reflects variations in the amount and extent of molecular gas between individual galaxies.
- We put the first constraints on the redshift evolution of the Cosmic dense-gas mass density, which tentatively increases by a factor of 7.4 ± 6.0 between $z = 0$ and $z \approx 2.5$. This trend is consistent with the evolution of the total molecular gas mass density if ≈3.5% of the total molecular gas is in the high-density regime.

This work opens a new chapter in studies of dense gas and star formation in early galaxies. As is underlined by the large number of detections, systematic surveys of dense gas in early galaxies with ALMA and NOEMA – aided by gravitational lensing – are now feasible. Systematic studies of dense gas across cosmic time can provide a powerful benchmark for upcoming cosmological hydrodynamical simulations that directly include cold, dense gas (e.g. COLIBRE, Schaye et al. 2025). Future observations will allow us to extend these studies to larger samples and down to sub-galactic scales.

Acknowledgements. The authors thank Z. Zhang for sharing the data from Zhang et al. (2014) and providing valuable insights into the local dense-gas observations. This work is based on observations carried out under project numbers S21CB and S23CB with the IRAM NOEMA Interferometer. IRAM is supported by INSU/CNRS (France), MPG (Germany) and IGN (Spain). The research leading to these results has received funding from the European Union's Horizon 2020 research and innovation programme under grant agreement No 101004719 [ORP]. This paper makes use of the following ALMA data: #2016.1.00663.S, #2017.1.01694.S, #2018.1.00747.S, and #2023.1.00432.S. ALMA is a partnership of ESO (representing its member states), NSF (USA) and NINS (Japan), together with NRC (Canada), MOST and ASIAA (Taiwan), and KASI (Republic of Korea), in cooperation with the Republic of Chile. The Joint ALMA Observatory is operated by ESO, AUI/NRAO and NAOJ. The authors acknowledge assistance from Allegro, the European ALMA Regional Center node in the Netherlands. M.R. is supported by the NWO Veni project "*Under the lens*" (VI.Veni.202.225). J.A.H. acknowledges support from the ERC Consolidator Grant 101088676 (VOYAJ). D.R. gratefully acknowledges support from the Collaborative Research Center 1601 (SFB 1601 sub-projects C1, C2, C3, and C6) funded by the Deutsche Forschungsgemeinschaft (DFG) – 500700252. T.R.G. is grateful for support from the Carlsberg Foundation via grant No. CF20-0534. S.V. acknowledges support from the European Research Council (ERC) grant MOPPEX ERC-833460. The Cosmic Dawn Center (DAWN) is funded by the Danish National Research Foundation under grant No. 140.

References

Aalto, S., Monje, R., & Martín, S. 2007, A&A, 475, 479
Amvrosiadis, A., Wardlow, J. L., Birkin, J. E., et al. 2025, MNRAS, 536, 3757
Baan, W. A., Henkel, C., Loenen, A. F., Baudry, A., & Wiklind, T. 2008, A&A, 477, 747
Barcos-Muñoz, L., Leroy, A. K., Evans, A. S., et al. 2017, ApJ, 843, 117
Béthermin, M., Greve, T. R., De Breuck, C., et al. 2018, A&A, 620, A115

[10] In the inner regions of nearby galaxies, the HCN and HCO$^+$ lines are usually moderately optically thick, with an optical depth of 1–2 (e.g. Jiménez-Donaire et al. 2017).

Bigiel, F., Leroy, A. K., Blitz, L., et al. 2015, ApJ, 815, 103
Boger, G. I., & Sternberg, A. 2005, ApJ, 632, 302
Bollo, V., Péroux, C., Zwaan, M., et al. 2025, A&A, 695, A163
Bussmann, R. S., Narayanan, D., Shirley, Y. L., et al. 2008, ApJ, 681, L73
Bussmann, R. S., Pérez-Fournon, I., Amber, S., et al. 2013, ApJ, 779, 25
Butler, K. M., van der Werf, P. P., Rybak, M., et al. 2021, ApJ, 919, 5
Butterworth, J., Viti, S., & Wang, Y. 2025, A&A, 697, A18
Calistro Rivera, G., Hodge, J. A., Smail, I., et al. 2018, ApJ, 863, 56
Cañameras, R., Nesvadba, N. P. H., Guery, D., et al. 2015, A&A, 581, A105
Cañameras, R., Yang, C., Nesvadba, N. P. H., et al. 2018, A&A, 620, A61
Cañameras, R., Nesvadba, N. P. H., Kneissl, R., et al. 2021, A&A, 645, A45
Carilli, C. L., Solomon, P., Vanden Bout, P., et al. 2005, ApJ, 618, 586
Casey, C. M., Zavala, J. A., Spilker, J., et al. 2018, ApJ, 862, 77
Costagliola, F., Aalto, S., Rodriguez, M. I., et al. 2011, A&A, 528, A30
Dame, T. M., & Lada, C. J. 2023, ApJ, 944, 197
Danielson, A. L. R., Swinbank, A. M., Smail, I., et al. 2013, MNRAS, 436, 2793
Dessauges-Zavadsky, M., Richard, J., Combes, F., et al. 2019, Nat. Astron., 3, 1115
Dudzevičiūtė, U., Smail, I., Swinbank, A. M., et al. 2020, MNRAS, 494, 3828
Dunne, L., Maddox, S. J., Papadopoulos, P. P., Ivison, R. J., & Gomez, H. L. 2022, MNRAS, 517, 962
Evans, N. J., II, Kim, K.-T., Wu, J., et al. 2020, ApJ, 894, 103
Falgarone, E., Zwaan, M. A., Godard, B., et al. 2017, Nature, 548, 430
Forbrich, J., Lada, C. J., Pety, J., & Petitpas, G. 2023, MNRAS, 525, 5565
Frayer, D. T., Harris, A. I., Baker, A. J., et al. 2011, ApJ, 726, L22
Frias Castillo, M., Rybak, M., Hodge, J., et al. 2022, ApJ, 930, 35
Frias Castillo, M., Hodge, J., Rybak, M., et al. 2023, ApJ, 945, 128
Fujimoto, S., Silverman, J. D., Bethermin, M., et al. 2020, ApJ, 900, 1
Gallagher, M. J., Leroy, A. K., Bigiel, F., et al. 2018, ApJ, 858, 90
Gao, Y., & Solomon, P. M. 2004a, ApJ, 606, 271
Gao, Y., & Solomon, P. M. 2004b, ApJS, 152, 63
Gao, Y., Carilli, C. L., Solomon, P. M., & Vanden Bout, P. A. 2007, ApJ, 660, L93
García-Burillo, S., Usero, A., Alonso-Herrero, A., et al. 2012, A&A, 539, A8
Ginolfi, M., Jones, G. C., Béthermin, M., et al. 2020, A&A, 633, A90
Giulietti, M., Lapi, A., Massardi, M., et al. 2023, ApJ, 943, 151
Graciá-Carpio, J., García-Burillo, S., Planesas, P., & Colina, L. 2006, ApJ, 640, L135
Graciá-Carpio, J., García-Burillo, S., Planesas, P., Fuente, A., & Usero, A. 2008, A&A, 479, 703
Graninger, D. M., Herbst, E., Öberg, K. I., & Vasyunin, A. I. 2014, ApJ, 787, 74
Greve, T. R., Papadopoulos, P. P., Gao, Y., & Radford, S. J. E. 2009, ApJ, 692, 1432
Gruppioni, C., Pozzi, F., Rodighiero, G., et al. 2013, MNRAS, 432, 23
Gruppioni, C., Béthermin, M., Loiacono, F., et al. 2020, A&A, 643, A8
Gullberg, B., Swinbank, A. M., Smail, I., et al. 2018, ApJ, 859, 12
Gullberg, B., Smail, I., Swinbank, A. M., et al. 2019, MNRAS, 490, 4956
Hacar, A., Bosman, A. D., & van Dishoeck, E. F. 2020, A&A, 635, A4
Hagimoto, M., Bakx, T. J. L. C., Serjeant, S., et al. 2023, MNRAS, 521, 5508
Harikane, Y., Ouchi, M., Oguri, M., et al. 2023, ApJS, 265, 5
Harrington, K. C., Weiss, A., Yun, M. S., et al. 2021, ApJ, 908, 95
Harris, A. I., Baker, A. J., Frayer, D. T., et al. 2012, ApJ, 752, 152
Henkel, C., & Mauersberger, R. 1993, A&A, 274, 730
Hodge, J. A., & da Cunha, E. 2020, Roy. Soc. Open Sci., 7, 200556
Hodge, J. A., Swinbank, A. M., Simpson, J. M., et al. 2016, ApJ, 833, 103
Ikeda, R., Tadaki, K.-I., Mitsuhashi, I., et al. 2025, A&A, 693, A237
Imanishi, M., Nakanishi, K., & Izumi, T. 2018a, ApJ, 856, 143
Imanishi, M., Nakanishi, K., Izumi, T., & Wada, K. 2018b, ApJ, 853, L25
Impellizzeri, C. M. V., Gallimore, J. F., Baum, S. A., et al. 2019, ApJ, 884, L28
Iono, D., Hatsukade, B., Kohno, K., et al. 2012, PASJ, 64, L2
Israel, F. P. 2023, A&A, 671, A59
Ivison, R. J., Papadopoulos, P. P., Smail, I., et al. 2011, MNRAS, 412, 1913
Izumi, T., Kohno, K., Aalto, S., et al. 2016, ApJ, 818, 42
Jiménez-Donaire, M. J., Bigiel, F., Leroy, A. K., et al. 2017, MNRAS, 466, 49
Jiménez-Donaire, M. J., Bigiel, F., Leroy, A. K., et al. 2019, ApJ, 880, 127
Jiménez-Donaire, M. J., Usero, A., Bešlić, I., et al. 2023, A&A, 676, L11
Jin, M., Lee, J.-E., & Kim, K.-T. 2015, ApJS, 219, 2
Jones, G. H., Clark, P. C., Glover, S. C. O., & Hacar, A. 2023, MNRAS, 520, 1005
Juneau, S., Narayanan, D. T., Moustakas, J., et al. 2009, ApJ, 707, 1217
Kauffmann, J., Goldsmith, P. F., Melnick, G., et al. 2017, A&A, 605, L5
Kazandjian, M. V., Meijerink, R., Pelupessy, I., Israel, F. P., & Spaans, M. 2015, A&A, 574, A127
Kelly, B. C. 2007, ApJ, 665, 1489
Kohno, K. 2003, ASP Conf. Ser., 289, 349
König, S., Aalto, S., Muller, S., et al. 2018, A&A, 615, A122
Krips, M., Neri, R., García-Burillo, S., et al. 2008, ApJ, 677, 262
Krumholz, M. R., & McKee, C. F. 2005, ApJ, 630, 250
Krumholz, M. R., & Thompson, T. A. 2007, ApJ, 669, 289
Lagos, C. D. P., da Cunha, E., Robotham, A. S. G., et al. 2020, MNRAS, 499, 1948
Li, F., Wang, J., Fang, M., et al. 2020, PASJ, 72, 41
Lutz, D., Berta, S., Contursi, A., et al. 2016, A&A, 591, A136
Madau, P., & Dickinson, M. 2014, ARA&A, 52, 415
Magnelli, B., Elbaz, D., Chary, R. R., et al. 2011, A&A, 528, A35
Martín, S., Mangum, J. G., Harada, N., et al. 2021, A&A, 656, A46
Massardi, M., Enia, A. F. M., Negrello, M., et al. 2018, A&A, 610, A53
Meijerink, R., Spaans, M., & Israel, F. P. 2007, A&A, 461, 793
Narayanan, D., Cox, T. J., Shirley, Y., et al. 2008, ApJ, 684, 996
Negrello, M., Hopwood, R., De Zotti, G., et al. 2010, Science, 330, 800
Negrello, M., Amber, S., Amvrosiadis, A., et al. 2017, MNRAS, 465, 3558
Neumann, L., Gallagher, M. J., Bigiel, F., et al. 2023, MNRAS, 521, 3348
Nguyen, Q. R., Jackson, J. M., Henkel, C., Truong, B., & Mauersberger, R. 1992, ApJ, 399, 521
Nishimura, Y., Aalto, S., Gorski, M. D., et al. 2024, A&A, 686, A48
Onus, A., Krumholz, M. R., & Federrath, C. 2018, MNRAS, 479, 1702
Oteo, I., Zhang, Z. Y., Yang, C., et al. 2017, ApJ, 850, 170
Papadopoulos, P. P. 2007, ApJ, 656, 792
Papadopoulos, P. P., Zhang, Z.-Y., Xilouris, E. M., et al. 2014, ApJ, 788, 153
Planck Collaboration XIII. 2016, A&A, 594, A13
Privon, G. C., Herrero-Illana, R., Evans, A. S., et al. 2015, ApJ, 814, 39
Privon, G. C., Ricci, C., Aalto, S., et al. 2020, ApJ, 893, 149
Rangwala, N., Maloney, P. R., Glenn, J., et al. 2011, ApJ, 743, 94
Reuter, C., Spilker, J. S., Vieira, J. D., et al. 2023, ApJ, 948, 44
Riechers, D. A., Walter, F., Carilli, C. L., et al. 2006, ApJ, 645, L13
Riechers, D. A., Walter, F., Cox, P., et al. 2007, ApJ, 666, 778
Riechers, D. A., Weiß, A., Walter, F., & Wagg, J. 2010, ApJ, 725, 1032
Riechers, D. A., Hodge, J., Walter, F., Carilli, C. L., & Bertoldi, F. 2011, ApJ, 739, L31
Riechers, D. A., Pavesi, R., Sharon, C. E., et al. 2019, ApJ, 872, 7
Romano, D., & Matteucci, F. 2003, MNRAS, 342, 185
Romano, D., Matteucci, F., Zhang, Z. Y., Papadopoulos, P. P., & Ivison, R. J. 2017, MNRAS, 470, 401
Rybak, M., Calistro Rivera, G., Hodge, J. A., et al. 2019, ApJ, 876, 112
Rybak, M., Hodge, J. A., Vegetti, S., et al. 2020, MNRAS, 494, 5542
Rybak, M., Hodge, J. A., Greve, T. R., et al. 2022, A&A, 667, A70
Rybak, M., van Marrewijk, J., Hodge, J. A., et al. 2023, A&A, 679, A119
Rybak, M., Jansen, J. T., Frias Castillo, M., et al. 2025, A&A, 700, A278
Sabatini, G., Bovino, S., Giannetti, A., et al. 2021, A&A, 652, A71
Sage, L. J., Mauersberger, R., & Henkel, C. 1991, A&A, 249, 31
Saintonge, A., & Catinella, B. 2022, ARA&A, 60, 319
Sakamoto, K., Aalto, S., Evans, A. S., Wiedner, M. C., & Wilner, D. J. 2010, ApJ, 725, L228
Salim, D. M., Alatalo, K., Federrath, C., Groves, B., & Kewley, L. J. 2020, ApJ, 893, 26
Salpeter, E. E. 1955, ApJ, 121, 161
Schaye, J., Chaikin, E., Schaller, M., et al. 2025, ArXiv e-prints [arXiv:2508.21126]
Schinnerer, E., & Leroy, A. K. 2024, ARA&A, 62, 369
Serjeant, S. 2012, MNRAS, 424, 2429
Solomon, P., Vanden Bout, P., Carilli, C., & Guelin, M. 2003, Nature, 426, 636
Spilker, J. S., Marrone, D. P., Aguirre, J. E., et al. 2014, ApJ, 785, 149
Stanley, F., Jones, B. M., Riechers, D. A., et al. 2023, ApJ, 945, 24
Stuber, S. K., Pety, J., Usero, A., et al. 2025, A&A, 696, A182
Tacconi, L. J., Genzel, R., Saintonge, A., et al. 2018, ApJ, 853, 179
Tacconi, L. J., Genzel, R., & Sternberg, A. 2020, ARA&A, 58, 157
Tan, Q.-H., Gao, Y., Zhang, Z.-Y., et al. 2018, ApJ, 860, 165
Tunnard, R., Greve, T. R., Garcia-Burillo, S., et al. 2015, ApJ, 815, 114
Usero, A., Leroy, A. K., Walter, F., et al. 2015, AJ, 150, 115
Valtchanov, I., Virdee, J., Ivison, R. J., et al. 2011, MNRAS, 415, 3473
van der Vlugt, D., Hodge, J. A., Algera, H. S. B., et al. 2022, ApJ, 941, 10
Vanden Bout, P. A., Solomon, P. M., & Maddalena, R. J. 2004, ApJ, 614, L97
Viti, S. 2017, A&A, 607, A118
Vollmer, B., Freundlich, J., Gratier, P., et al. 2025, A&A, 693, A267
Wagg, J., Wilner, D. J., Neri, R., Downes, D., & Wiklind, T. 2005, ApJ, 634, L13
Walter, F., Carilli, C., Neeleman, M., et al. 2020, ApJ, 902, 111
Wardlow, J. L., Cooray, A., Osage, W., et al. 2017, ApJ, 837, 12
Wilson, C. D., Petitpas, G. R., Iono, D., et al. 2008, ApJS, 178, 189
Wilson, C. D., Bemis, A., Ledger, B., & Klimi, O. 2023, MNRAS, 521, 717
Wu, J., Evans, N. J., Gao, Y., et al. 2005, ApJ, 635, L173
Yang, C., Omont, A., Beelen, A., et al. 2017, A&A, 608, A144
Yang, C., Omont, A., Martín, S., et al. 2023, A&A, 680, A95
Zavala, J. A., Casey, C. M., Manning, S. M., et al. 2021, ApJ, 909, 165
Zhang, Z.-Y., Gao, Y., Henkel, C., et al. 2014, ApJ, 784, L31
Zhang, Z.-Y., Romano, D., Ivison, R. J., Papadopoulos, P. P., & Matteucci, F. 2018, Nature, 558, 260

Appendix A: Details of NOEMA and ALMA observations

Table A.1 summarises the details of NOEMA and ALMA observations.

Table A.1. Observations summary. Individual columns list: target ID, dates of observations, HCN transition targeted, on-source time, synthesised beam FWHM and position angle, and rms noise over a 100 km s^{-1} bandwidth at the position of the HCN line.

Target	Transitions	Date	t_{on} [h]	Beam FWHM & PA [arcsec^2, deg]	$\sigma_{100\,km/s}$ [mJy/beam]
		NOEMA			
J1202	(3–2)	2021 August 26	2.6	5.6×4.8 (56)	0.32
J1202	(4–3)	2021 August 29	3.4	5.1×4.0 (88)	0.35
SDP.130	(3–2)	2021 Sep 20, Dec 23; 2022 Jan 16	1.9	4.7×2.5 (68)	0.26
J0209	(3–2)	2021 August 13	5.3	7.5×5.0 (35)	0.42
SDP.9	(4–3)	2023 October 6	3.4	2.6×0.9 (13)	0.39
SDP.11	(4–3)	2023 October 8	4.5	3.5×1.1 (11)	0.43
		ALMA			
G09v1.40	(3–2)	2018 April 9	0.86	2.7×2.1 (154)	0.14
SDP.17	(4–3)	2018 April 26, May 1, May 2	1.03	2.1×1.6 (23)	0.21
SDP.130	(4–3)	2018 April 9, April 24	0.89	2.4×1.8 (153)	0.11
G09v1.326	(4–3)	2018 April 22	0.91	2.1×2.0 (143)	0.14
G12v2.43	(4–3)	2018 April 3	0.84	2.4×2.2 (22)	0.13
NAv1.195	(4–3)	2018 March 30, April 26	1.69	2.8×1.7 (86)	0.20
G15v2.235	(4–3)	2018 April 6	0.47	2.3×1.9 (29)	0.18

Appendix B: Imaging and spectra

Figures B.1 and B.2 present synthesised images of the continuum for individual sources, obtained with NOEMA and ALMA, respectively. For NOEMA observations, we show images for the upper and lower sideband separately.

Figures B.3 and B.4 present the narrow-band images for the HCN, HCO$^+$, and HNC lines for individual sources. Finally, Fig. B.5 and B.5 present the spectra extracted for individual sources. Table B.1 lists the fluxes for individual tracers inferred from the mom-0 maps.

Table B.1. Line flux measurements from moment-0 images, not corrected for the lensing magnification.

Source	HCN(4–3) [Jy km/s]	HCO$^+$(4–3) [Jy km/s]	HNC(4–3) [Jy km/s]
SDP.130	0.15±0.05	≤0.13	0.09±0.05
SDP.17	0.45±0.09	0.29±0.09	0.47±0.10
SDP.9	1.62±0.18	1.56±0.18	1.25±0.20
SDP.11	0.54±0.22	≤0.62	≤0.42
G09v1.326	0.15±0.11	0.18±0.13	0.24±0.12
G12v2.43	0.44±0.04	0.32±0.04	0.47±0.04
G15v2.235	≤0.24	≤0.24	≤0.27
NAv1.195	0.43±0.12	0.39±0.10	≤0.7
J1202	0.93±0.23	1.01±0.24	≤0.66
Source	HCN(3–2) [Jy km/s]	HCO$^+$(3–2) [Jy km/s]	HNC(3–2) [Jy km/s]
G09v1.140	0.24±0.04	0.28±0.04	0.20±0.04
SDP.130	≤0.43	≤0.38	≤0.38
J0209	1.77±0.23	1.00±0.23	1.30±0.20
J1202	1.44±0.21	1.40±0.21	0.56±0.21

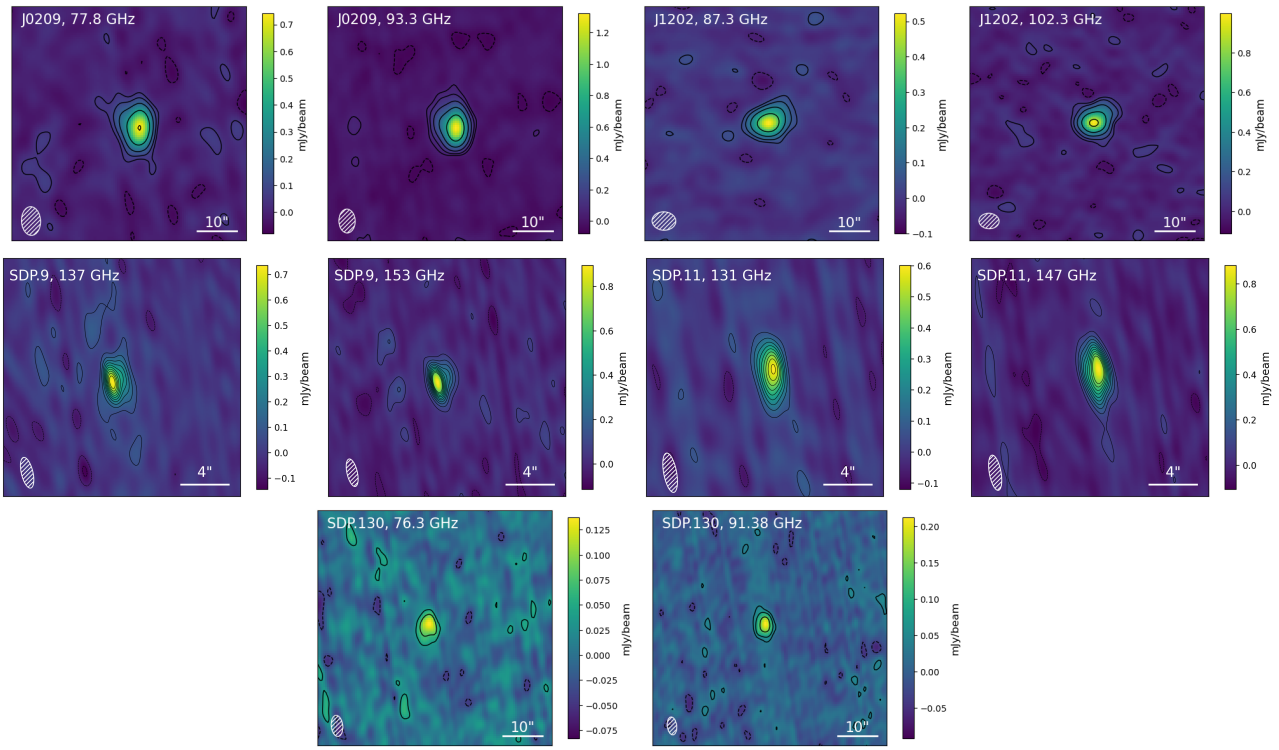

Fig. B.1. NOEMA Band 1/2 continuum imaging of individual galaxies. The observed-frame frequencies are given in each panel. For each target, we show separate images for the lower and upper sidebands. All images were produced using natural weighting. Contours start at $\pm 2\sigma$ and terminate at 20σ, with a 2σ increment. All sources are detected in the continuum emission and are marginally resolved.

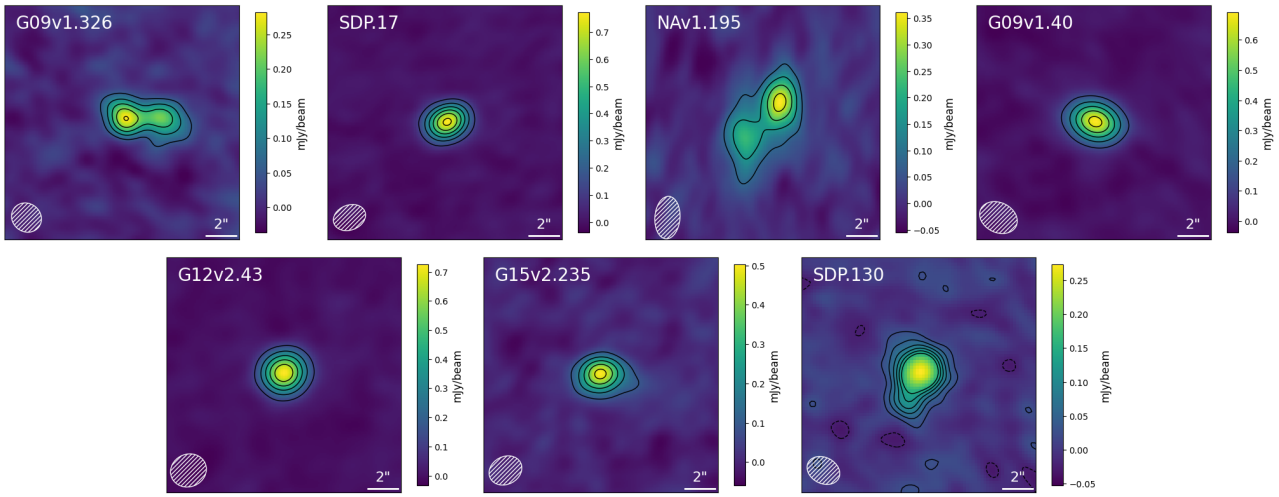

Fig. B.2. ALMA Band 3/4 continuum imaging of our targets. All images were produced using natural weighting. Contours start at $\pm 2\sigma$, with a 2σ increment. All sources are clearly detected in the continuum emission. G09v1.326 and NAv1.195 are resolved into two point-like sources due to the lensing morphology. SDP.130 is blended with a fainter galaxy (at a different redshift) to the south-west.

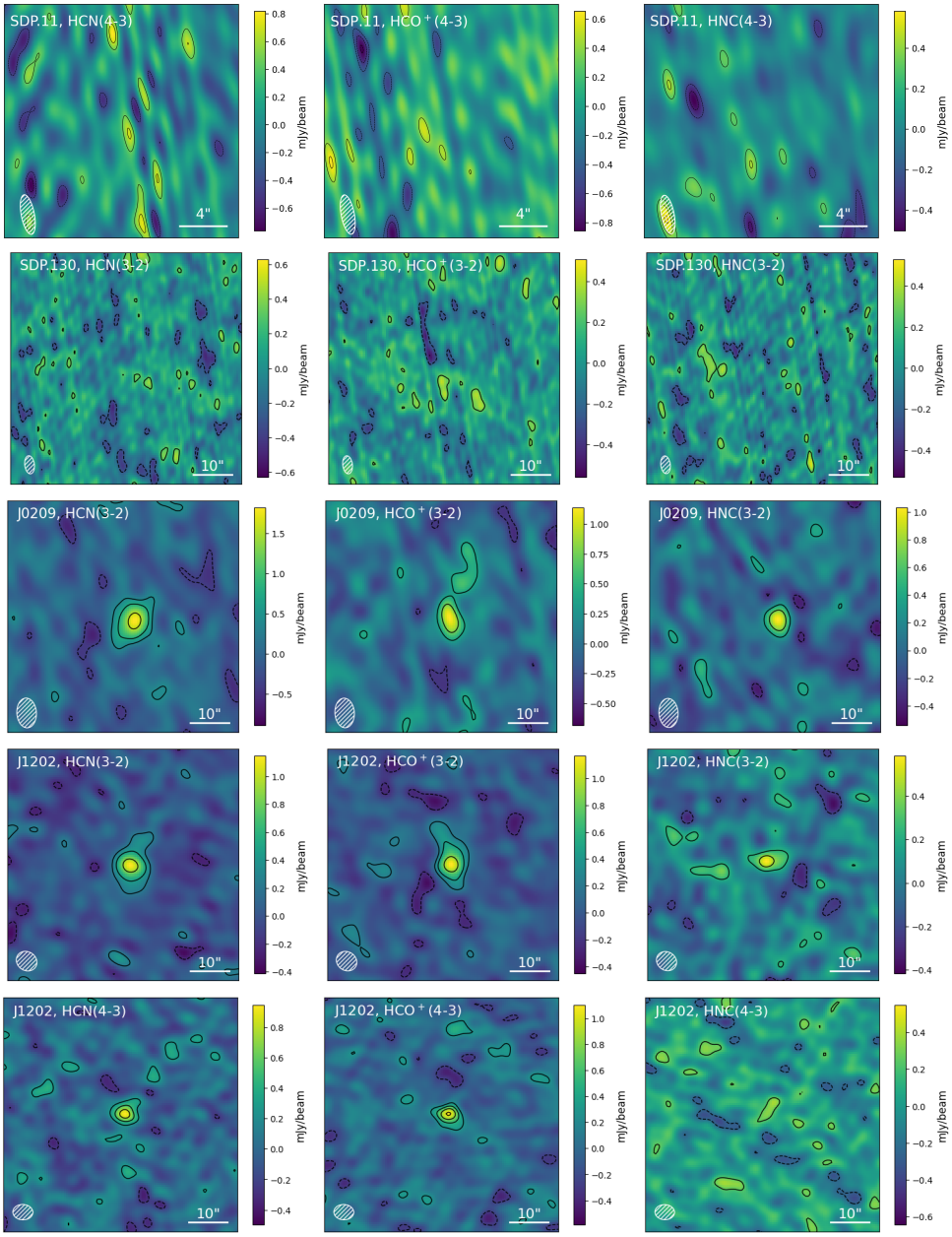

Fig. B.3. Figure 2 continued: NOEMA narrow-band images of the HCN/HCO$^+$/HNC lines in individual sources. The field of view is 20"*times*20"; contours start at $\pm 2\sigma$ and increase in steps of 2σ. J0209 is clearly detected in all lines except HCN(4–3), J1202 is detected in all transitions. SDP.130 is not detected in any transition.

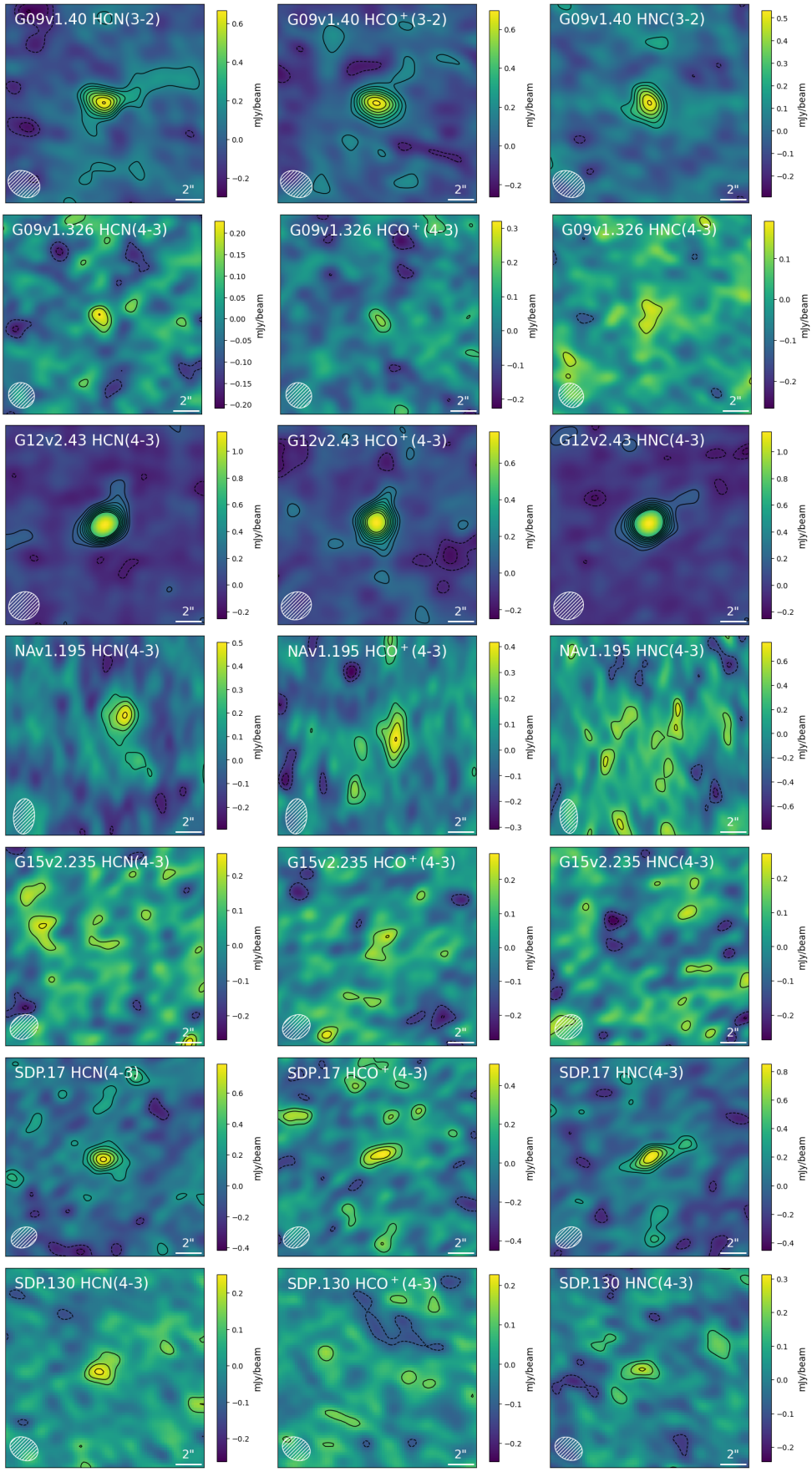

Fig. B.4. Figure 2 continued: ALMA narrow-band images of the HCN/HCO$^+$/HNC lines for individual sources. Contours are drawn at $\pm(2,3,...10)\sigma$.

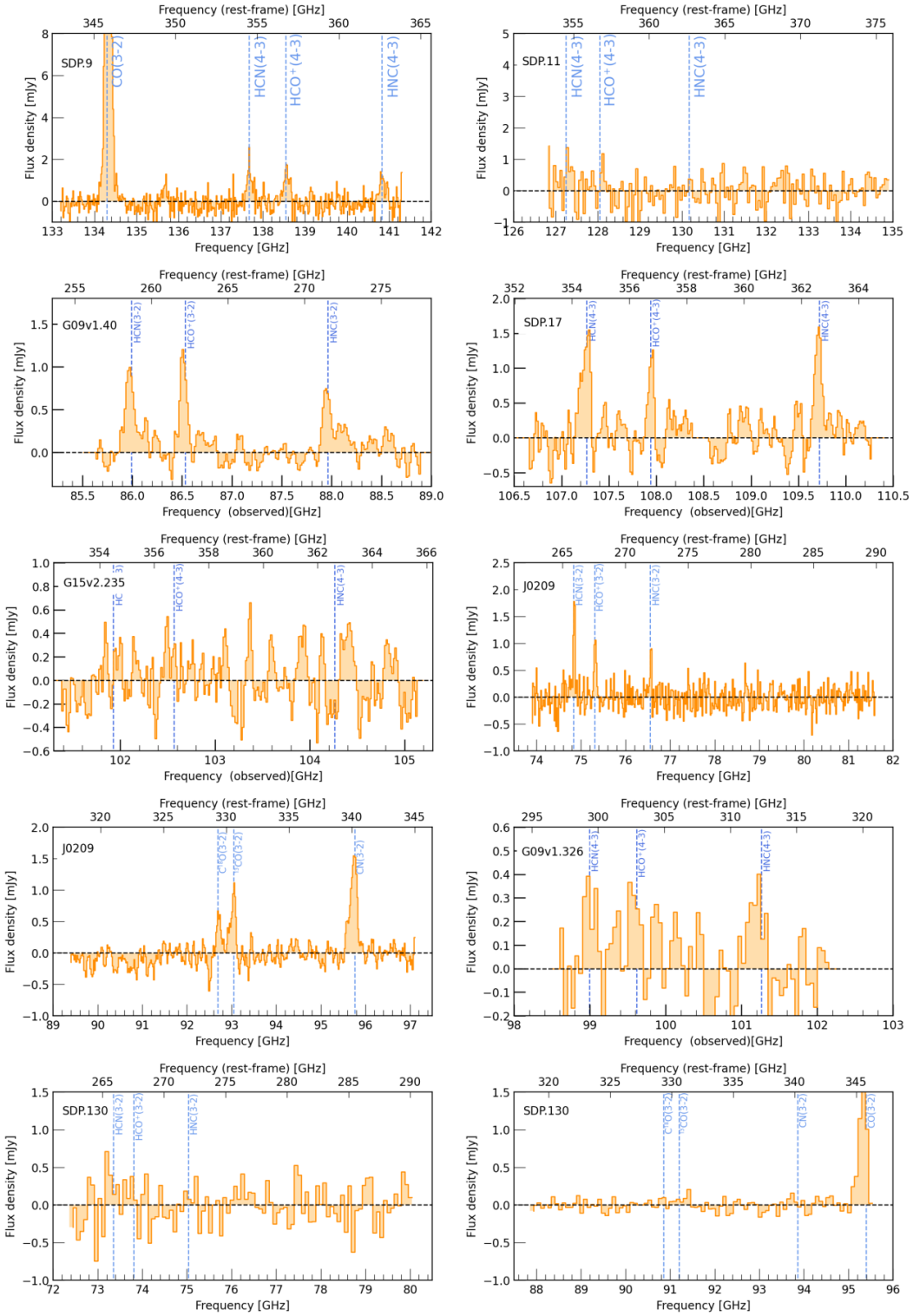

Fig. B.5. Spectra for individual targets, after continuum subtraction. In SDP.9, we detect HCN, HCO^+, and HNC(4–3) lines. For SDP.11, no lines are detected. In J0209, besides HCN, HCO^+, and HNC, we also detect the ^{13}CO, $C^{18}O$ and CN emission. We do not detect any dense-gas tracers in SDP.130. Note the blue-shifted HCN(3–2) emission in G09v1.40, which might be coming from a molecular outflow.

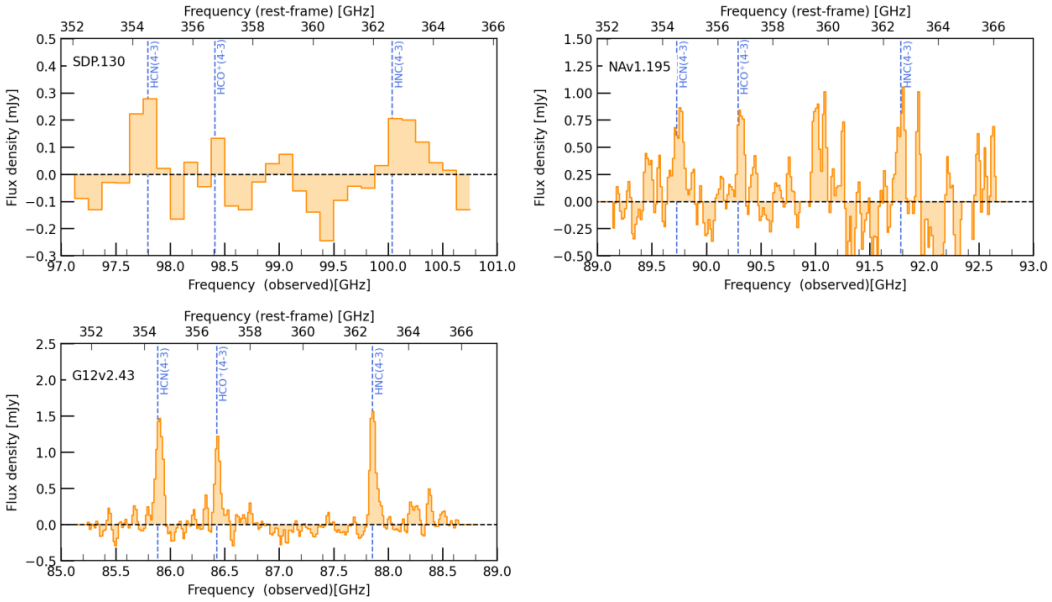

Fig. B.5. continued.

Appendix C: Detections of CO isotopologues: ^{13}CO and C^{18}O

In J0209 and J1202, our NOEMA spectral setup covers the CO(3–2) isotopologues ^{13}CO(3–2) (f_0 = 330.588 GHz) and C^{18}O(3–2) (f_0 = 329.331 GHz). As is shown in Fig. D.1, we detect both transitions in both sources; the measured fluxes and luminosities are reported in Tab. D.1. The ^{13}CO/C^{18}O isotopologues luminosity ratios in J0209 and J1202 are $L'_{^{13}\mathrm{CO}}/L'_{\mathrm{C}^{18}\mathrm{O}}$=1.8±0.6 and 1.1±0.1, respectively. These are consistent with previous results for high-redshift DSFGs by (Zhang et al. 2018; Yang et al. 2023), and with the lower limit from the Spilker et al. (2014) spectral stack (^{13}CO/C^{18}O(3–2)≥1.1).

The ^{13}CO/C^{18}O ratio has been proposed as a potentially sensitive tracer of the IMF in obscured galaxies (e.g. Sage et al. 1991; Henkel & Mauersberger 1993; Romano & Matteucci 2003; Romano et al. 2017). This is because ^{13}C and ^{18}O are produced and dispersed via different routes. Namely ^{13}CO is primarily produced by low/intermediate-mass stars and novae ($M_\star \leq 8\,M_\odot$), whereas C^{18}O production is dominated by high-mass stars. In the Milky Way, ^{13}CO/C^{18}O luminosity ratio is ≈7 (Romano et al. 2017); lower ^{13}CO/C^{18}O ratios would thus indicate an excess of massive stars - a top-heavy IMF. Indeed, previous studies of CO isotopologues in DSFGs by Zhang et al. (2018), Yang et al. (2023) have found ratios close to unity. Taken at the face value, CO isotopologue ratios in J0209 and J1202 are consistent with a top-heavy IMF. However, there are considerable uncertainties in linking CO isotopologue ratios to the IMF slope, particularly when stellar rotation is taken into account (C. Kobayashi, priv. comm.)

Appendix D: Detections of CN

In J0209 and J1202, we obtain strong detection of the cyanide radical CN(N = 3 − 2) transition (with different fine- and hyperfine structure transition spanning f_0 = 339.447 − 340.279 GHz). CN arises primarily from regions exposed to strong ultraviolet (UV) or X-ray radiation (e.g. Boger & Sternberg 2005; Meijerink et al. 2007) The total flux of the CN(3–2) transitions is 2.9±0.3 Jy km/s in J1202 and 3.7±0.2 Jy km/s in J1202 (Tab. D.1), which corresponds to $L'_{\mathrm{CN(3-2)}} = (1.0 \pm 0.1) \times 10^{11}$ and $L'_{\mathrm{CN(3-2)}} = (1.2 \pm 0.1) \times 10^{11}$ K km s^{-1} pc^2, respectively.

Adopting the CO(3–2) luminosities from Harrington et al. (2021), we find CN(3–2)/CO(3–2) luminosity ratios of 0.15±0.04 and 0.17±0.05, respectively. These are comparable to measurements for the Cloverleaf quasar at z = 2.5 (CN(3–2)/CO(3–2) ratio of 0.11±0.02 (Riechers et al. 2007), but significantly higher than values reported for NCv1.143 (CN/CO=0.06, Yang et al. 2023) and for the spectral stack of SPT-selected galaxies (0.04, Reuter et al. 2023). Curiously, the CN(3–2) luminosities in J0209 and J1202 are about twice that of HCN(3–2) line (CN/HCN=1.8±0.3 and 2.0±0.4, respectively), in contrast to nearby star-forming galaxies, which show an almost-constant CN/HCN ratio of 0.86 ± 0.27 (Wilson et al. 2023).

Table D.1. Flux densities of CO isotopologues and CN transitioms in J0209 and J1202, in units of Jy km/s. The reported fluxes are not corrected for lensing magnification.

Source	^{13}CO(3–2)	C^{18}O(3–2)	CN(3–2)
J0209	0.77±0.14	0.43±0.13	2.9±0.3
J1202	1.77±0.11	1.61±0.14	3.7±0.2

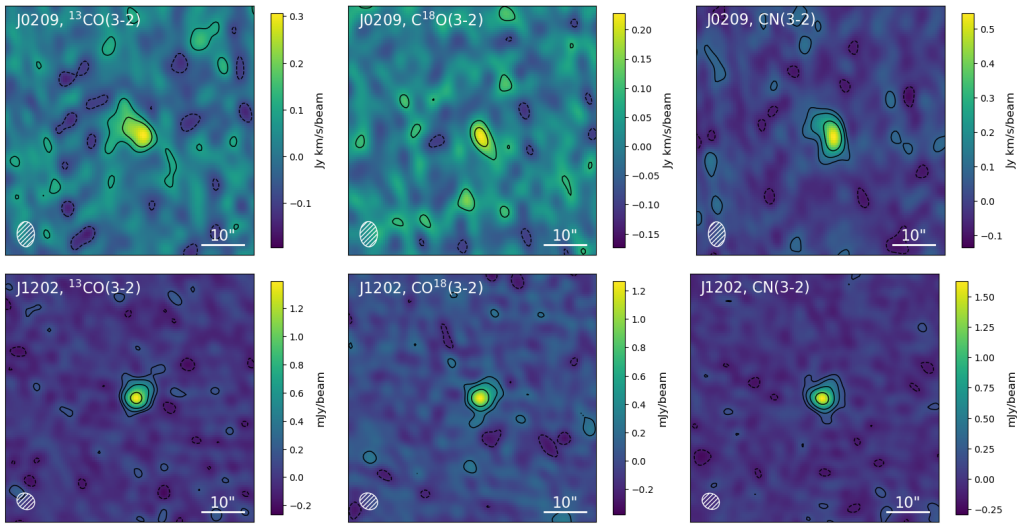

Fig. D.1. Detections of CO isotopologues and CN lines in J0209 and J1202. Contours start at ±2σ and increase in steps of 2σ.